NASA

MEMORANDUM

FLUID-DYNAMIC PROPERTIES OF SOME SIMPLE SHARP- AND

BLUNT-NOSED SHAPES AT MACH NUMBERS FROM

16 TO 24 IN HELIUM FLOW

By Arthur Henderson, Jr., and Patrick J. Johnston

Langley Research Center
Langley Field, Va.

NATIONAL AERONAUTICS AND SPACE ADMINISTRATION
WASHINGTON
June 1959

NATIONAL AERONAUTICS AND SPACE ADMINISTRATION

MEMORANDUM 5-8-59L

FLUID-DYNAMIC PROPERTIES OF SOME SIMPLE SHARP- AND

BLUNT-NOSED SHAPES AT MACH NUMBERS FROM

16 TO 24 IN HELIUM FLOW

By Arthur Henderson, Jr., and Patrick J. Johnston

SUMMARY

The fluid-dynamic characteristics of flat plates, 5° and 10° wedges, and 5° and 10° cones have been investigated at Mach numbers from 16.3 to 23.9 in helium flow. The flat-plate results are for a leading-edge Reynolds number range of 584 to 19,500 and show that the induced pressure distribution is essentially linear with the hypersonic viscous interaction parameter $\overline{X}$ within the scope of this investigation. It is also shown that the rate at which the induced pressure varies with $\overline{X}$ is a linear function of the leading-edge Reynolds number.

The wedge and cone results show that as the flow-deflection angle increases, the induced-pressure effects decrease and the measured pressures approach those predicted by inviscid shock theory.

INTRODUCTION

The induced effects of boundary-layer displacement thickness on the pressure distribution of a flat plate at hypersonic speeds were first pointed out in reference 1. Since that time numerous theoretical and experimental investigations have been made in an attempt to define and predict the induced pressure effects on simple configurations at hypersonic speeds.

The theoretical investigations presented in the literature have proceeded in two distinct phases. In the first phase pure viscous effects on flat plates were investigated by assuming an infinitesimally thin leading edge. The influence of the rate of growth of the hypersonic boundary layer on the pressure distribution was then determined by various methods, as reported in references 2 to 5, among others. These references included treatment of both the "weak" and "strong" interaction regions. The weak interaction region is far enough downstream of the leading edge that interaction between the flow field and boundary layer

is negligible and the surface streamwise pressure gradient is small; the strong interaction region is close to the leading edge where shock-wave—boundary-layer interactions are strong, and the boundary layer is in a high negative streamwise pressure gradient. These investigations have shown that the controlling parameter for the pressure distribution in both the weak and strong viscous interaction regions is the viscous hypersonic interaction parameter of reference 3.

In the second phase of the theoretical work pure inviscid effects on flat plates due to the finite leading-edge thickness were investigated. A theoretical model of the flow is reported in reference 6, wherein the inviscid flow about a flat plate with blunt leading edge is represented by flow about a flat plate with sonic-wedge leading edge, and the surface pressure variation is then determined by the method of characteristics. The effect of the large entropy gradient behind the curved shock is included by retaining the rotational term in the characteristics equation.

The inviscid effects caused by a blunt leading edge have also been treated in references 7 and 8 by use of the blast-wave theory based on the work of reference 9. The characteristic solution of reference 6 is shown to be correlated by the controlling parameter predicted by blast-wave theory (ref. 10).

Concurrently with the aforementioned theoretical work, the experimental work contained in references 2, 6, and 11 to 21 has been published. Within the range of variables covered, these investigations have generally tended to confirm the theoretical predictions for both the pure viscous and pure inviscid effects.

In the practical case, viscous and inviscid effects will exist simultaneously, however. Reference 16 presents a semiempirical, iterative procedure which attempts to account for the combined viscous and inviscid effects. However, the results are not suitable for making rapid engineering estimates. References 6 and 21 show by comparison with experiment that a simple linear addition of viscous and inviscid theories gives a good approximation to experiment within the scope of the available data.

The present investigation is an extension and amplification of the experimental work reported in reference 20. The Mach number was extended from 16.3 to 23.9 and the flat plates and cones were tested for a wide range of leading-edge or nose Reynolds numbers. The wedges were tested at one leading-edge Reynolds number only. The results are compared with theory.

At the Mach numbers of this test, which are in the satellite and space-vehicle reentry range, the viscous and inviscid effects are greatly

magnified so that a closer scrutiny of the various theoretical predictions as compared with experimental reality is possible.

SYMBOLS

A   constant (see eq. (7))

$$B = \frac{d}{dx}\left(\frac{\Delta p}{p_l}\right)$$

C   linear viscosity coefficient in relation $\frac{\mu_w}{\mu_l} = C \frac{T_w}{T_l}$; determined

                 from $C = \left(1 + \frac{\gamma - 1}{2} M^2\right)^{\omega - 1}$ for $N_{Pr} = 1$

$C_{D,n}$ nose drag coefficient

d   nose diameter, in.

d*   throat diameter, in.

M   Mach number

N_{Pr} Prandtl number

p   static pressure, lb/sq in.

p_c inviscid pressure on cone surface at nose, lb/sq in.

p_t total pressure, lb/sq in.

Δp induced static pressure (measured pressure minus reference pressure)

R   Reynolds number

R_d Reynolds number based on nose diameter

R_t Reynolds number based on leading-edge thickness

R_x Reynolds number based on distance from leading edge

r	radial distance from center line of tunnel
T	temperature, $^{\circ}R$
T_t	total temperature, $^{\circ}R$
T_w	wall temperature, $^{\circ}R$
t	leading-edge thickness, in.
w	width of plate, in.
x	distance from leading edge of model, in.
x_{th}	distance from throat of nozzle, in.
γ	ratio of specific heats
θ	semicone or semiwedge angle, deg
μ	dynamic viscosity, lb/in-sec
$\overline{X}$	hypersonic viscous interaction parameter, $\dfrac{M^3\sqrt{C}}{\sqrt{R_x}}$
ω	viscosity power-law index in relation $\dfrac{\mu_w}{\mu_l} = \left(\dfrac{T_w}{T_l}\right)^{\omega}$

Subscripts:

1	free-stream conditions at leading edge or nose
2	conditions behind normal shock
i	inviscid
l	local inviscid condition
m	measured
T	theoretical
v	viscous
w	inviscid conditions on wedge surface at leading edge

APPARATUS

All tests were performed in a 2-inch-diameter helium blowdown tunnel located in the Langley 9-Inch Tunnel Section. A diagram of the tunnel and its operating components is shown in figure 1. The tunnel has two interchangeable throats of 0.052- and 0.060-inch diameter. The conical nozzle expands with a semidivergence angle of 5° from the throat to the constant 2-inch-diameter section. Helium was supplied from a 55-cubic-foot reservoir to the tunnel stagnation chamber at pressures up to 3,000 lb/sq in. The tunnel could be operated for 10 minutes at a stagnation pressure of 2,000 lb/sq in. A two-stage steam ejector was used to create a low back pressure; the ratio of stagnation pressure to back pressure was practically constant over a wide range of stagnation pressure and was about 1,000 and 1,300 for the 0.060- and 0.052-inch-diameter throats, respectively. The stagnation temperature was constant for any given test and always in the range of 79° F to 94° F.

Visual observations of the models were made in a second 2-inch tunnel which was identical to the first except that it was equipped with schlieren windows. The tunnel with the schlieren windows used the same two interchangeable throats.

The test models were supported by means of a long sting whose longitudinal position was controlled by a motorized gear and screw system. The sting was centered in the tunnel by two spiders and the clamp on the longitudinal control mechanism. The orifice locations and dimensions on the test models are shown in figure 2. The orifices were all 0.020 inch in diameter.

Tunnel Calibration

The calibration of the axisymmetric tunnel with each of the available throats is presented in figure 3.

In the boundary layer the pitot pressure is less than free-stream pressure, and behind a shock it is greater than free-stream pressure. If the pitot pressures obtained in the boundary layer and behind a shock are used to compute a Mach number from the total-pressure ratio across a normal shock, assuming isentropic flow from the stagnation chamber up to the normal shock, the indicated Mach number will be wrong. The computation will indicate Mach numbers which are higher than free-stream values in the boundary layer and lower than free-stream values behind a shock. These may be seen in figure 3. The beginning of incorrect Mach number indications is the limit of the usable flow. Figure 4 was prepared from figure 3(a) and shows the approximate usable region in the tunnel with $d^* = 0.052$ inch and $p_{t,1} = 2,015$ lb/sq in. abs.

The 0.052-inch-diameter throat which was used for most of these tests was more thoroughly calibrated than the other throat. The lateral Mach number distribution is better with the 0.060-inch throat than with the 0.052-inch throat; however, the Mach number capability is not as high. The effect of the lateral Mach number distribution was determined by testing a flat plate with $t = 0.009$ inch and $w = 0.8$ inch at the same Mach number and total pressure with both throats. The results are shown in figure 5. The agreement of the data in the two different throats indicates that, so long as the center-line Mach numbers and stagnation pressures are the same, a small lateral Mach number variation has a negligible effect on the model center-line pressure.

The difference in lateral Mach number gradients with the two throats is attributed to the difference in the growth of the tunnel-wall boundary layers. When the smaller of the two throats is used, the unit Reynolds number will be less at each tunnel station for constant stagnation pressure. Thus, the boundary layer at any station will be thicker when $d^* = 0.052$ inch than when $d^* = 0.060$ inch. At the nozzle exit the thicker boundary layer presents a greater region of subsonic flow through which downstream back-pressure effects may be propagated. The forward feeding of downstream pressure disturbances aggravates the situation by increasing the boundary-layer thickness still more, in some cases causing separation and breakdown of flow. The boundary layer also affects the location of the shock which, in the absence of viscosity, would originate on the wall of the tunnel at the cone-cylinder juncture. This interaction of the shock and boundary layer also affects the condition of the boundary layer.

The effect of varying the unit Reynolds number of the flow is illustrated in figure 6, which shows the variation of the Mach number at $r = 0.3$ inch at a fixed station in the tunnel (with $d^* = 0.060$ inch). The Reynolds number variation was obtained by varying the stagnation pressure. As $p_{t,1}$ decreases, the Mach number decreases, indicating that the wall boundary layer is increasing in thickness.

Instrumentation

Supply and pitot pressures were measured on Bourdon gages with an accuracy of ± 5 and ± 0.1 lb/sq in., respectively. Static pressures were read on U-tube butyl phthalate manometers. The reference pressure on the U-tubes was maintained at less than 20 microns of mercury. Twenty microns of mercury is equivalent to approximately 0.01-inch of butyl phthalate, which was considered to be within the reading accuracy of the U-tubes. The estimated accuracy of the measured static pressures is ± 0.0007 lb/sq in.

The estimated accuracy in Mach number, based on the aforementioned combined errors, is given in the following table:

$p_{t,1}$, lb/sq in.	Maximum percentage error in M at -			
	M = 17	M = 19	M = 21	M = 23
1,015	±0.9	±1.2	±1.5	----
1,515	±.6	±.8	±1.0	±1.3
2,015	±.5	±.5	±.8	±1.0

TESTS

For all tests, the models were alined along the tunnel center line at zero angle of attack and zero angle of yaw. The free-stream Mach number was varied by changing the longitudinal position of the model in the tunnel in accordance with the calibration curves of figure 3. The variation of the Reynolds number based on leading-edge thickness was attained by varying the stagnation pressure from 1,015 to 2,015 lb/sq in. abs and by varying the leading-edge thickness of the various models. The leading-edge thickness for the flat plates and wedges and the nose diameter for the cones are given in figure 2. Most of the flat plates were 0.8 inch wide, but some plates 0.6 inch wide were tested to determine the effect of plate width. The surface static pressures were photographically recorded at the steady-state condition, which was usually obtained about 90 to 120 seconds after the tunnel was started.

RESULTS AND DISCUSSION

Schlieren Observations

Schlieren photographs are presented in figures 7 to 9 for some of the configurations tested. All pictures are for a stagnation pressure of 2,015 lb/sq in. abs. For the flat plate, only the 0.001- and 0.020-inch-thick leading edge is shown, and for the wedge only the 0.002-inch-thick leading edge was tested. The cone photographs also show only the smallest and largest nose diameters. No pressure measurements were made on the cones with a nose diameter of 0.002 inch.

8

The effect of leading-edge thickness on the condition of the boundary layer on the flat plate, as well as the effect on the shock shape, is very marked. (See fig. 7.) For the sharp flat plate (t = 0.001 inch) two features are immediately noticeable: (1) the presence of the strong shock caused by the rapid growth of the boundary layer at the leading edge which, in the absence of viscosity, would be a Mach wave, and (2) the white streak between the plate surface and the shock, which denotes the edge of the thermal boundary layer. The shock inclination indicates that $T_2/T_1 \approx 5$ in the inviscid flow region, while recovery temperature exists at the plate surface. Thus the ratio of wall temperature to the temperature of the inviscid flow external to the boundary layer is on the order of 20 to 30.

On the blunt flat plate the shock is obviously detached and much steeper than the shock for the sharp plate. Also, the region indicating high thermal shear does not occur on the schlieren photographs of the blunt flat plate. In fact, there is no indication of the presence of a thick boundary layer. The temperature rise across the strong shock has increased the temperature of the inviscid flow over the plate to a level much closer to the recovery temperature, and the boundary layer is thus similar to that for low supersonic conditions.

For the sharp-leading-edge wedges shown in figure 8 the edge of the thermal gradient, which is essentially the edge of the boundary layer, is closer to the surface than in the case of the flat plates alined with the stream. This thinning of the boundary layer is a consequence of the change in local conditions (mainly local Mach number and local Reynolds number). With increasing angle of attack the predictions of inviscid shock theory will become increasingly more accurate.

The sharp-nosed cones show the same characteristics as the wedges; the steeper the cone angle, the closer the edge of the thermal boundary layer lies to the surface. (See fig. 9.) Also, the flow field behind the detached shock from the blunt-nosed cones shows no white streak, as was the case with the blunt flat plates.

Reference Pressure

Although there was a longitudinal Mach number gradient in the tunnel, no attempt was made to correct the data for any effect the gradient may have had. For the flat plates, the reference pressure was the leading-edge free-stream static pressure; for the wedges and cones, the reference pressure was calculated from the inviscid shock equations and the free-stream static pressure at the leading edge or nose.

The reason no attempt was made to correct the data is that, at high Mach numbers, shock-reflected disturbances play a minor role in determining body surface pressures compared with the effect of disturbances generated by the body (including boundary-layer displacement thickness) except near shock detachment. (See refs. 22 and 23.) That is, the pressure distribution on a body is determined primarily by the initial shock at the nose and by the Prandtl-Meyer expansions over the body itself. There is no reason to believe that a Mach number gradient external to the shock will make the shock-reflected disturbances become important except, perhaps, under some rather extreme conditions.

In reference 20 the flat-plate data are corrected for the Mach number gradient by taking as the reference pressure the free-stream static pressure that would have existed at each orifice location when the tunnel was empty. The value of $\overline{X}$ is also determined at each orifice for tunnel-empty conditions.

The method used to handle the flat-plate data in the present report and the method used in reference 20 are compared in figure 10, which is a plot of $\Delta p/p_1$ against $\overline{X}_1$ (method of present report) and $\Delta p/p_l$ against $\overline{X}_l$ (method of ref. 20) for a high and a low value of R_t at $M_1 = 17$ and $M_1 = 23$. It can be seen that the two methods give essentially the same results. Thus the data of the present paper and the data of reference 20 are directly comparable.

Flat-Plate Results

The flat-plate pressure distributions are presented in figures 11 and 12 as $\Delta p/p_1$ against $\overline{X}_1$ for various values of R_t and M_1. The main body of the data is presented in figure 11 and is for $w = 0.8$ inch. The data shown in figure 12 are for $w = 0.6$ inch and include a repeat of some of the data shown in figure 11 in order to show that width effect was apparently unimportant in the range of the present tests.

Consistently high readings were obtained from the second and last orifices of the plate whose leading edge was blunted to obtain thicknesses of $t = 0.001$, 0.002, 0.0035, and 0.008 inch. These points are not presented. The other leading-edge thicknesses were obtained on different plates.

The variation of $\Delta p/p_1$ with $\overline{X}_1$ in figures 11 and 12 is seen to be essentially linear for all tests. The slope and location of the curves vary with both Mach number and R_t. The curves on figures 11 and 12 should not be extrapolated beyond $\overline{X}_1 \approx \dfrac{M_1{}^3 \sqrt{C}}{2 \sqrt{R_t}}$ for $R_t > 6{,}000$, as will be shown later.

Comparison of Data With Various Theoretical Predictions

For the thinnest leading edge, where the inviscid effects are minimized, the agreement of the data with Lees' zeroth-order strong-interaction theory (ref. 4) is fairly good. (See fig. 11.) As R_t increases, the deviation of the data above Lees' curve increases until, at $M_1 = 23$, $\overline{X}_1 = 23$, and $R_t = 11,680$, the value of $\Delta p/p_1$ reaches 55 as compared with 20 for the viscous prediction. For this case the interaction is predominantly due to inviscid effects. The difference in the character of the flow may be seen in the schlieren photographs of figure 7.

Since all the plates tested had finite leading-edge thicknesses, both viscous and inviscid effects are present in all the data. Although there is as yet no complete theoretical treatment of the combined viscous and inviscid effects, including possible interaction effects, reference 16 presents a semiempirical iterative procedure for determining the combined viscous and inviscid effects. However, the method does not appear suitable for making rapid engineering estimates. References 6 and 21 indicate that a good prediction of the pressure distribution on a real flat plate (where both viscous and inviscid effects exist simultaneously) can be obtained by a linear addition of the viscous and inviscid theoretical pressures. In the comparison to be made with the present data, the viscous solution is taken to be the strong interaction solution of reference 4:

$$\left(\frac{\Delta p}{p_1}\right)_v = 0.92\overline{X}_1 - 1 \tag{1}$$

and the inviscid solution is taken to be the blast-wave solution of reference 7:

$$\left(\frac{\Delta p}{p_1}\right)_i = 0.169\left(\frac{M_1^3 C_{I,N}}{x/t}\right)^{2/3} \tag{2}$$

At high values of M_1, the value of $C_{D,N}$ for a flat, two-dimensional nose normal to the free stream is given in reference 4 as

$$C_{D,N} = \frac{\gamma + 3}{\gamma + 1} \tag{3}$$

where relieving effects at the edge of the nose are neglected.

Thus, for helium

$$\left(\frac{\Delta p}{p_1}\right)_i = 0.246 M_1^2 \left(\frac{t}{x}\right)^{2/3} \qquad (4)$$

For the flat plate, equation (4) can be rewritten as a function of $\bar{x}_1$:

$$\left(\frac{\Delta p}{p_1}\right)_i = 0.246 \left(\frac{R_t}{C}\right)^{2/3} \frac{\bar{x}_1^{4/3}}{M_1^2} \qquad (5)$$

This equation is plotted in figure 13 for various values of M_1 and R_t.

A linear addition of equations (1) and (5) gives

$$\left(\frac{\Delta p}{p_1}\right)_{i+v} = \left[0.246 \left(\frac{R_t}{C}\right)^{2/3} \frac{\bar{x}_1^{1/3}}{M_1^2} + 0.92\right]\bar{x}_1 - 1 \qquad (6)$$

Equation (6) is seen to account for all the variables which the experimental data of figures 11 and 12 show to be important, including R_t, although the predicted nonlinearity of the pressure ratio with $\bar{x}_1$ is not found in the data. However, since the nonlinearity of $\Delta p / p_1$ with $\bar{x}_1$ shown in equation (6) is fairly weak, equation (6) should still give a good approximation.

Figure 14 has been prepared in order to determine the range of applicability of $\left(\Delta p / p_1\right)_v$, $\left(\Delta p / p_1\right)_i$, and $\left(\Delta p / p_1\right)_{i+v}$ (from eqs. (1), (5), and (6)) with respect to the present data. The figure indicates that equation (1) is most satisfactory in the low R_t range, as would be expected, and gives good results for $0 < R_t < 2,000$. Equation (6) is superior to the other two for $2,000 < R_t < 4,000$, while for $4,000 < R_t < 7,000$ equations (5) and (6) yield roughly the same degree of approximation. Equation 5 is best in the range $7,000 < R_t < 20,000$; that is, when R_t is greater than 7,000, the experimental results are predicted with good accuracy by a purely inviscid theory. Note that equation (6) always gives conservative results, and is thus useful for making first approximations regardless of the R_t range.

Empirical Analysis of Flat-Plate Data

The experimental data show $\Delta p/p_1$ to be linear in $\bar{X}_1$; that is,

$$\frac{\Delta p}{p_1} = A + B\bar{X}_1 \qquad (7)$$

It is therefore of interest to examine the nature of B, the coefficient of $\bar{X}_1$. To gain some insight into the controlling parameters, the slopes of the faired curves of figures 11 and 12 were measured and are plotted in figure 15 as B against R_t, where $B = \frac{d}{d\bar{X}_1}\left(\frac{\Delta p}{p_1}\right)$. Although there is considerable scatter, the plotted points can be approximately represented by two distinct straight lines:

$$B \approx 0.6 + \frac{R_t}{3,600} \qquad (0 < R_t < 6,000) \quad (8)$$

$$B \approx 1.6 + \frac{R_t}{9,300} \qquad (6,000 < R_t < 20,000) \quad (9)$$

Thus, the data indicate that the coefficient of $\bar{X}_1$ is roughly linear in R_t and independent of M_1, at least within the scope of this investigation. Empirically, then, the flat-plate pressure distributions are found to be approximately represented by

$$\frac{\Delta p}{p_1} = A + \left(0.6 + \frac{R_t}{3,600}\right)\bar{X}_1 \qquad (0 < R_t < 6,000) \qquad (10)$$

and

$$\frac{\Delta p}{p_1} = A + \left(1.6 + \frac{R_t}{9,300}\right)\bar{X}_1 \qquad (6,000 < R_t < 20,000) \qquad (11)$$

It should be noted that the limit of applicability of equation (11) is $\bar{X}_1 \approx \frac{M_1{}^3\sqrt{C}}{2\sqrt{R_t}}$ because the pressure-distribution pattern shown in figures 11 and 12 (and 16) breaks down when x/t is less than about 3 or 4 as a result of the overexpansion and recompression immediately behind the shoulder of the blunt leading edge. (See ref. 17.) Thus, if x/t must be equal to or greater than 4, $\bar{X}_1 \lessgtr \frac{M_1{}^3\sqrt{C}}{2\sqrt{R_t}}$.

Equation (10) shows that as R_t approaches zero the empirically determined coefficient of $\bar{X}_1$ is roughly 0.6 for these data, rather than the theoretically determined constant of 0.92 (ref. 4).

No attempt was made to correlate the parameter A. It appeared to be subject to random scatter. Its contribution to $\Delta p/p_1$ will generally be small.

A comparison of equations (10) and (11) with equation (6) shows that although equation (6) predicts a variation of $\Delta p/p_1$ with $\bar{X}_1$ and R_t, the orders of magnitude of the variations are not quite correct. Also, the predicted variation of $\Delta p/p_1$ with M_1 is not realized, at least within the scatter of the data.

The reason for the abrupt change in slope of the data at $R_t \approx 6,000$ is not known, but it certainly indicates that a rapid change in the character of the flow is taking place. The abrupt change occurs close to the point ($R_t \approx 7,000$) at which the inviscid blast-wave theory becomes as accurate as or better than the sum of the viscous and inviscid predictions (fig. 14). In reference 15 it is stated that when R_t is greater than 4,000, the flow is independent of Reynolds number. (This conclusion is not strictly correct and was apparently reached because the data were plotted to an insensitive log-log scale.) This value of R_t is on the same order as that at which the present data indicate a rapid change in flow characteristic from viscid-inviscid to primarily inviscid.

Reference 18 presents pressure distributions on flat plates at Mach numbers of 11.4, 12.7, and 13.8 in helium. The R_t range was from 93 to 17,300, which is comparable to that of the present investigation. The data, which are presented as $\Delta p/p_l$ against x/t in reference 18, have been replotted as $\Delta p/p_1$ against $\bar{X}_1$ and are shown in figure 16. The data were taken from the log-log plots of reference 18 with the aid of a Gerber variable scale and a set of log tables. Values of $\Delta p/p_1$ were obtained from $\Delta p/p_l$ by use of the following equation:

$$\frac{\Delta p}{p_1} = \frac{p_l}{p_1}\left(\frac{\Delta p}{p_l} + 1\right) - 1 \tag{12}$$

The ratio p_l/p_1 was obtained from the Mach number distribution given in figure 3 of reference 15, together with the tables of reference 24. As in the present investigation, the variation of $\Delta p/p_1$ with $\overline{X}_1$ is seen to be essentially linear.

Values of B have been obtained from figure 16 and are shown in figure 17. Superimposed on this figure are equations (8) and (9), representing the results of the present investigation.

As in the present data, there is considerable scatter, particularly at the lower values of R_t. Of interest are the points above $R_t = 6,000$. They form a straight line which is approximately parallel to equation (9) but displaced above it, suggesting the presence of a Mach number effect of the type predicted by blast-wave theory, although not necessarily of the same order of magnitude. Further investigation is necessary to resolve this point. It is of interest to note that the type of variation found from reference 18 and the present investigation could be

roughly accounted for at $R_t > 6,000$ by setting $B \approx \dfrac{7.6}{\sqrt{M_1}} + \dfrac{R_t}{9,300}$.

Wedges

Although both 5° and 10° wedges were investigated, only the results for the 5° wedges are thought to be reliable. The small test core of the tunnel (see fig. 4) limited the model width to 0.8 inch for the 5° wedge and to 0.6 inch for the 10° wedge. This width was not great enough to prevent some pressure bleed-off on the 10° wedge. The effect was similar to, but not as marked as, that reported in reference 20. The wedges were tested at $M_1 = 21$ and 23 only and with $t = 0.002$ inch. Figure 18 presents a plot of $\Delta p/p_w$ against x, the distance from the leading edge, for the 5° and 10° wedges at $M_1 = 21$ and $R_t = 1,360$ to illustrate the type of distributions obtained. The highest pressure ratio shown for the 10° wedge is probably correct since it is close to the leading edge where side-edge effects should be negligible. The downstream orifices showed bleed-off effects, however, when the pressures were plotted against $\overline{X}_w$.

Although the effect of the boundary layer is clearly evident in figure 18, the magnitude of its effect on the pressures is much less than for the flat plates, and as the wedge angle increases, the measured pressures approach the pressures predicted by inviscid theory, as would be expected. The decreased dependence of pressure on the boundary layer as flow deflection angle increases is illustrated more clearly in

figure 19, which presents the data from figure 18 along with flat-plate data for the same values of M_1 and R_t.

Figure 20 presents $\Delta p/p_w$ for the 5° wedge plotted against $\bar{X}_w$. As for the flat plate, the distribution of the induced static-pressure ratio is linear in $\bar{X}_w$ and follows the second-order weak-interaction theory of reference 3 given by

$$\frac{\Delta p}{p_w} = 0.629\bar{X}_w + 0.152\bar{X}_w^{\,2} \tag{13}$$

only up to $\bar{X}_w = 1.5$ to 2. The viscous strong-interaction solution is parallel to the data and constitutes a good prediction when shifted the proper amount. Whether wedge pressures, like flat-plate pressures, are strongly dependent on R_t could not be determined here since R_t was not varied by a significant amount. However, the theoretical results of reference 21 show that R_t has an effect.

Figure 20 also shows that the average slope of $\Delta p/p_w$ against $\bar{X}_w$ is about 0.95, which is of the same magnitude as the values given by equation (8) for $R_t = 1,200$. (See fig. 15.)

Cones

The 5° and 10° cones were each tested with four different nose bluntnesses. The data are presented in figures 21 and 22 as $\Delta p/p_c$ against x/d. The results are compared with the theory of reference 25. This theory assumes a sharp cone $(R_d \approx 0)$; therefore it is not surprising that the deviation of experimental results from theory increases with increasing R_d. In general, theory and experiment agree fairly well for low R_d and high x/d, where the effect of the nose bluntness would be expected to be small. The reason for the large deviation of experiment from theory at $M_1 = 21$ and $R_d = 2,450$ and at $M_1 = 23$ and $R_d = 3,140$ for the 5° cone is not known. The overexpansion shown near the nose is similar to that reported in references 26 and 27. In the same manner as for the wedges, the inviscid prediction becomes better as the cone angle increases.

CONCLUSIONS

An aerodynamic investigation of flat plates, 5° and 10° wedges, and 5° and 10° cones in helium flow at Mach numbers from 16.3 to 23.9 indicates the following conclusions:

1. The induced pressure distribution on all the flat plates tested, covering a range of leading-edge Reynolds number R_t of 584 to 19,500, varied linearly with the hypersonic viscous interaction parameter $\overline{X}_1$ despite the fact that a linear variation is theoretically predicted only for the pure viscous $(R_t = 0)$ case in the strong-interaction region.

2. There are two distinct flow regimes whose character depends upon R_t. For $R_t \lesssim 6,000$ the flow is controlled by both viscous and inviscid phenomena and in this range a linear addition of viscous and inviscid theories constitutes a good first approximation to the experimental results. For $6,000 \lesssim R_t \lesssim 20,000$ the flow is primarily inviscid in nature, and in this region inviscid blast-wave theory alone gives a good approximation to the results. Transition from one regime to the other is rapid.

3. The rate at which the experimental induced flat-plate pressures varied with $\overline{X}_1$ was found to be a linear function of R_t. The function of R_t is different in the two regimes, however. When $R_t < 6,000$ the rate is about 2.5 times that for $R_t > 6,000$.

4. The results for the 5° wedge indicate that even in the weak viscous interaction region, the induced pressure variation is linear with $\overline{X}_w$ and is predicted by the second-order weak-interaction theory only over a limited range of $\overline{X}_w$.

5. The cone induced pressure prediction based on weak interaction theory is considered good for the sharp cones. As tip bluntness increases, the theory, which assumes a sharp nose, becomes less applicable. Although tip bluntness altered the pressure near the tip considerably, the effects did not persist many nose diameters downstream.

6. The effect of compressive flow deflection is to greatly decrease induced pressure effects of blunt leading edges in both viscous and inviscid flow. As wedge and cone angles increased the measured pressures approached the inviscid pressure prediction of two-dimensional or cone

shock theory. It is only at zero or small positive flow-deflection angles that induced-pressure effects are large.

Langley Research Center,
        National Aeronautics and Space Administration,
                Langley Field, Va., February 16, 1959.

REFERENCES

1. Becker, John V.: Results of Recent Hypersonic and Unsteady Flow Research at the Langley Aeronautical Laboratory. Jour. App. Phys., vol. 21, no. 7, July 1950, pp. 619-628.

2. Bertram, Mitchel H.: An Approximate Method for Determining the Displacement Effects and Viscous Drag of Laminar Boundary Layers in Two-Dimensional Hypersonic Flow. NACA TN 2773, 1952.

3. Lees, Lester, and Probstein, Ronald F.: Hypersonic Viscous Flow Over a Flat Plate. Rep. No. 195 (Contract AF 33(038)-250), Aero. Eng. Lab., Princeton Univ., Apr. 20, 1952.

4. Lees, Lester: Hypersonic Flow. GALCIT Pub. No. 404, 1955.

5. Lees, Lester: Influence of the Leading-Edge Shock Wave on the Laminar Boundary Layer at Hypersonic Speeds. Jour. Aero. Sci., vol. 23, no. 6, June 1956, pp. 594-600, 612.

6. Bertram, Mitchel H.: Viscous and Leading-Edge Thickness Effects on the Pressures on the Surface of a Flat Plate in Hypersonic Flow. Jour. Aero. Sci., vol. 21, no. 6, June 1954, pp. 430-431.

7. Cheng, H. K., and Pallone, A. J.: Inviscid Leading-Edge Effect in Hypersonic Flow. Jour. Aero. Sci. (Readers' Forum), vol. 23, no. 7, July 1956, pp. 700-702.

8. Lees, Lester, and Kubota, Toshi: Inviscid Hypersonic Flow Over Blunt-Nosed Slender Bodies. Jour. Aero. Sci., vol. 24, no. 3, Mar. 1957, pp. 195-202.

9. Taylor, Geoffrey.: The Formation of a Blast Wave by a Very Intense Explosion. I. Theoretical Discussion. II. The Atomic Explosion of 1945. Proc. Roy. Soc. (London), ser. A, vol. 201, no. 1065, Mar. 22, 1950, pp. 159-186.

10. Bertram, M. H., and Baradell, D. L.: A Note on the Sonic-Wedge Leading-Edge Approximation in Hypersonic Flow. Jour. Aero. Sci. (Readers' Forum), vol. 24, no. 8, Aug. 1957, pp. 627-628.

11. Kendall, James M., Jr.: An Experimental Investigation of Leading-Edge Shock-Wave - Boundary-Layer Interaction at Mach 5.8. Jour. Aero. Sci., vol. 24, no. 1, Jan. 1957, pp. 47-56.

12. Bertram, Mitchel H.: Boundary-Layer Displacement Effects in Air at Mach Numbers of 6.8 and 9.6. NACA TN 4133, 1958.

13. Creager, Marcus O.: Effects of Leading-Edge Blunting on the Local Heat Transfer and Pressure Distributions Over Flat Plates in Supersonic Flow. NACA TN 4142, 1957.

14. Hammitt, A. G., and Bogdonoff, S. M.: A Study of the Flow About Simple Bodies at Mach Numbers From 11 to 15. WADC Tech. Rep. 54-257, U. S. Air Force, Oct. 1954.

15. Hammitt, A. G., and Bogdonoff, S. M.: Hypersonic Studies of the Leading Edge Effect on the Flow Over a Flat Plate. Jet Propulsion, vol. 26, no. 4, Apr. 1956, pp. 241-246, 250.

16. Hammitt, Andrew G.: The Hypersonic Viscous Effect on a Flat Plate With Finite Leading Edge. Rep. No. 378 (WADC TN 57-105), Dept. Aero. Eng., Princeton Univ., Mar. 1957.

17. Vas, I. E., Bogdonoff, S. M., and Hammitt, A. G.: An Experimental Investigation of the Flow Over Simple Two-Dimensional and Axial Symmetric Bodies at Hypersonic Speeds. Rep. No. 382 (WADC TN 57-246), Dept. Aero. Eng., Princeton Univ., June 1957.

18. Vas, Irwin E.: An Experimental Investigation of the Pressure on a Thin Flat Plate at Hypersonic Speeds. Rep. No. 377 (WADC TN 57-104, AD 118151), Dept. Aero. Eng., Princeton Univ, Mar. 1957.

19. Munson, Albert G.: A Preliminary Experimental Investigation of the Flow Over Simple Bodies of Revolution at M = 18.4 in Helium. Memo. No. 35 (Army Ord. Contract No. DA-04-495-Ord-19), GALCIT, Dec. 15, 1956.

20. Erickson, Wayne D.: Study of Pressure Distributions on Simple Sharp-Nosed Models at Mach Numbers From 16 to 18 in Helium Flow. NACA TN 4113, 1957.

21. Bertram, Mitchel H., and Henderson, Arthur, Jr.: Effects of Boundary-Layer Displacement and Leading-Edge Bluntness on Pressure Distribution, Skin Friction, and Heat Transfer of Bodies at Hypersonic Speeds. NACA TN 4301, 1958.

22. Eggers, A. J., Jr., Savin, Raymond C., and Syvertson, Clarence A.: The Generalized Shock-Expansion Method and Its Application to Bodies Traveling at High Supersonic Air Speeds. Jour. Aero. Sci., vol. 22, no. 4, Apr. 1955, pp. 231-238, 248.

23. Eggers, A. J., Jr., Syvertson, Clarence A., and Kraus, Samuel: A Study of Inviscid Flow About Airfoils at High Supersonic Speeds. NACA Rep. 1123, 1953.

24. Mueller, James N.: Equations, Tables, and Figures for Use in the Analysis of Helium Flow at Supersonic and Hypersonic Speeds. NACA TN 4063, 1957.

25. Probstein, Ronald F.: Interacting Hypersonic Laminar Boundary Layer Flow Over a Cone. Tech. Rep. AF 2798/1 (Contract AF 33(616)-2798), Div. Eng., Brown Univ., Mar. 1955.

26. Bertram, Mitchel H.: Tip-Bluntness Effects on Cone Pressures at M = 6.85. Jour. Aero. Sci. (Readers' Forum), vol. 23, no. 9, Sept. 1956, pp. 898-900.

27. Chernyi, G. G.: Hypersonic Flow Around a Slender Blunt Cone. C-113, Morris D. Friedman, Inc. (Needham Heights 94, Mass.). (From Doklady Akademii Nank SSSR, vol. 115, no. 4, 1957, pp. 681-683.)
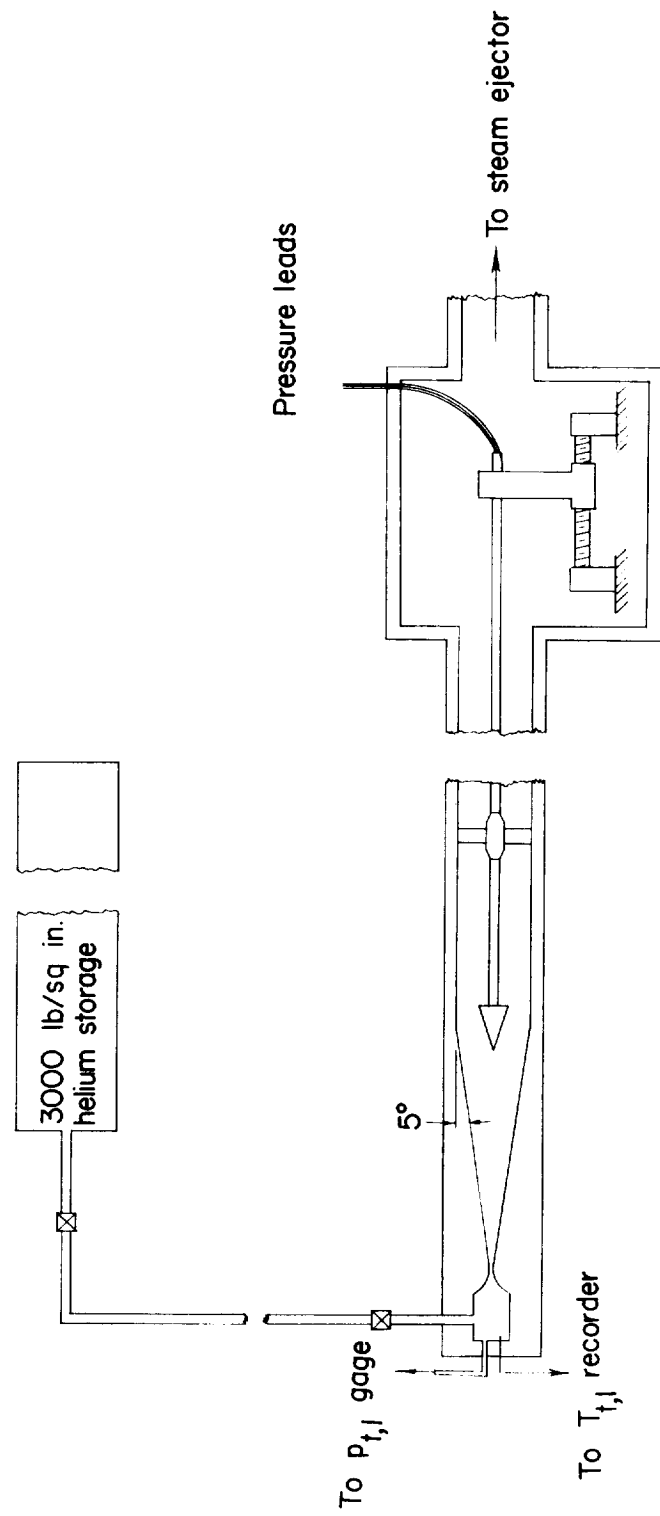
Figure 1.- Diagram of operating circuit of 2-inch helium tunnel.

Flat-Plate Orifice Locations

t	w	x_1	x_2	x_3	x_4	x_5
0.001	0.80	0.091	0.147	0.225	0.347	0.549
.002		.089	.145	.223	.345	.547
.0035		.086	.142	.220	.342	.544
.005		.093	.164	.241	.357	.557
.008		.076	.132	.210	.332	.534
.009		.095	.154	.232	.355	.555
.012		.090	.152	:232	.344	.544
.020		.078	.140	.220	.332	.532
.007	0.60	.101	.158	.241	.360	.552
.009		.095	.154	.232	.355	.555

Wedge Orifice Locations

θ, deg	t	w	l	x_1	x_2	x_3	x_4	x_5
5	0.002	0.80	1.75	0.184	0.308	0.402	0.602	0.800
10	.002	.60	.88	.080	.208	.306	.404	.606

Cone Orifice Locations

θ, deg	d	l	x_1	x_2	x_3	x_4	x_5
5	0.007	2.10	0.510	0.717	0.915	1.200	1.590
	.014	2.06	.475	.682	.880	1.165	1.555
	.029	1.97	.377	.584	.782	1.067	1.457
	.060	1.79	.197	.404	.602	.887	1.277
10	.005	1.04	.254	.411	.548	.708	.903
	.014	1.02	.234	.396	.526	.684	.876
	.028	.98	.190	.348	.486	.642	.826
	.060	.89	.098	.256	.390	.554	.750
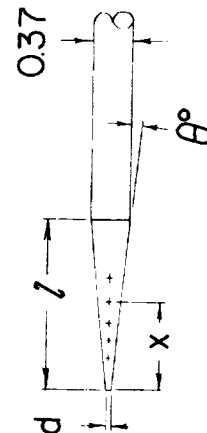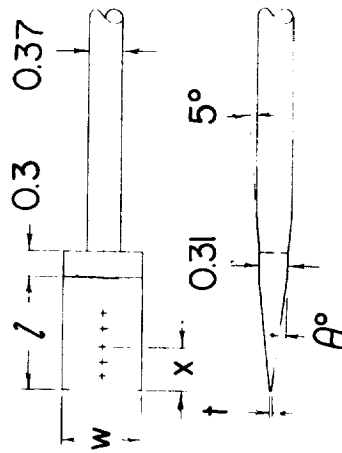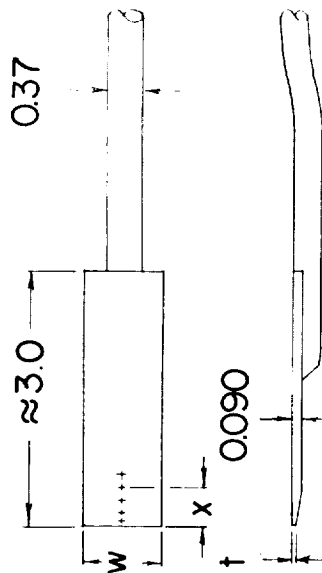
Figure 2.- Test models. All dimensions are in inches.
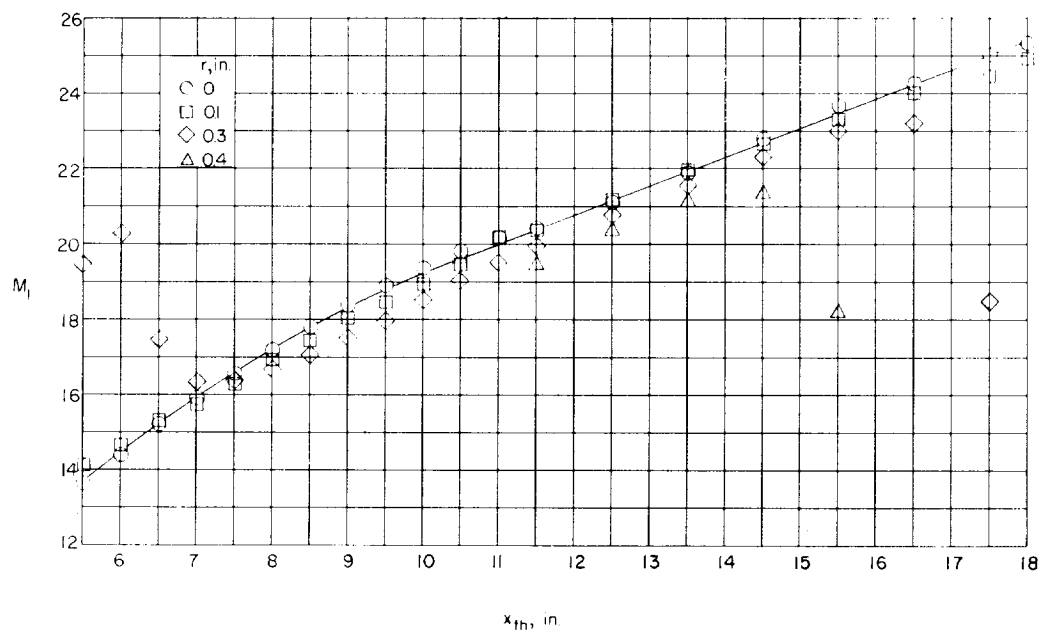
(a) d* = 0.052 inch; $p_{t,1}$ = 2,015 lb/sq in. abs.
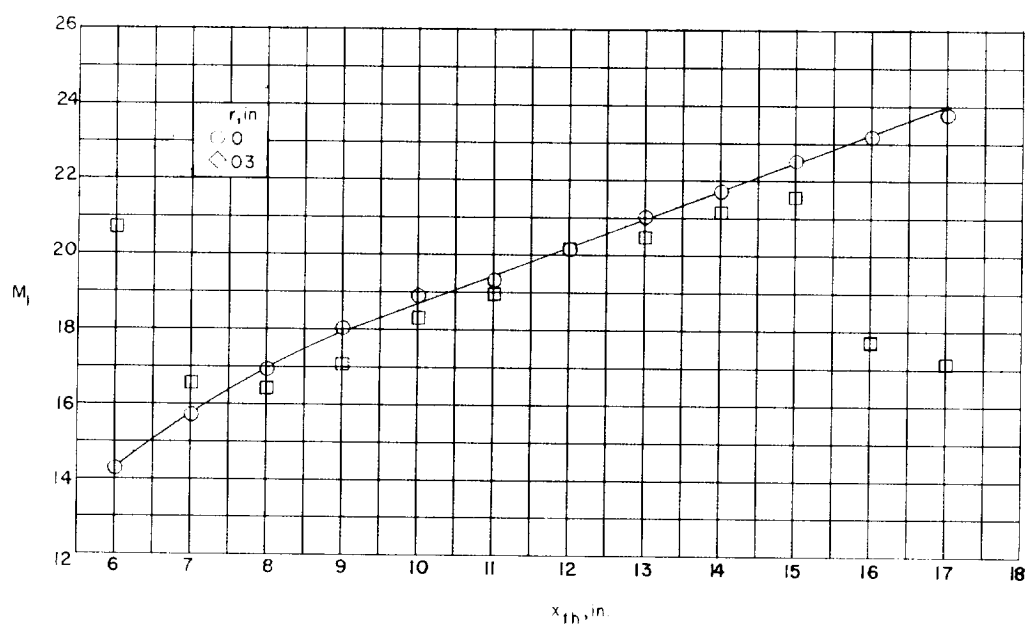
(b) d* = 0.052 inch; $p_{t,1}$ = 1,515 lb/sq in. abs.

Figure 3.- Mach number distribution in 2-inch helium nozzle.
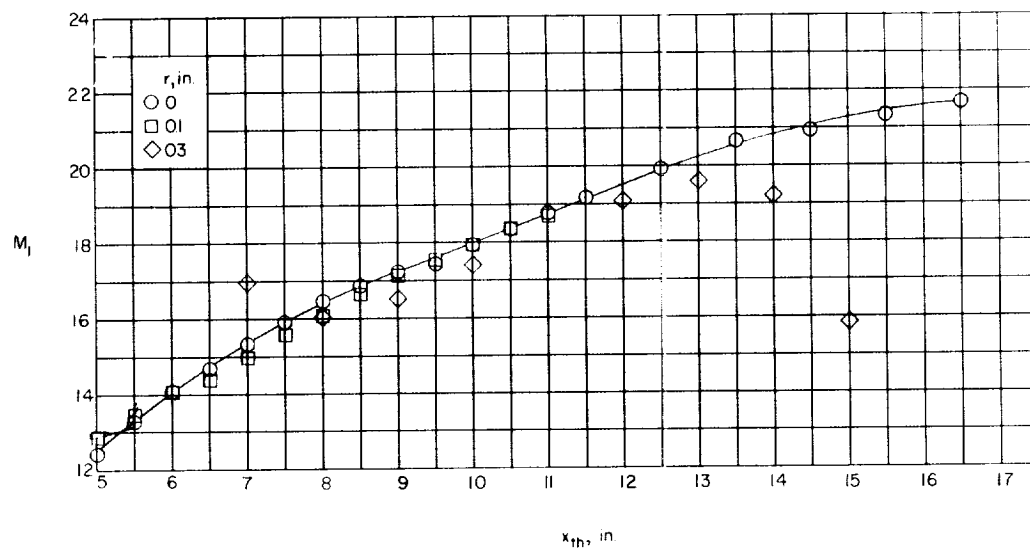
(c)   d* = 0.052 inch; $p_{t,1}$ = 1,015 lb/sq in. abs.
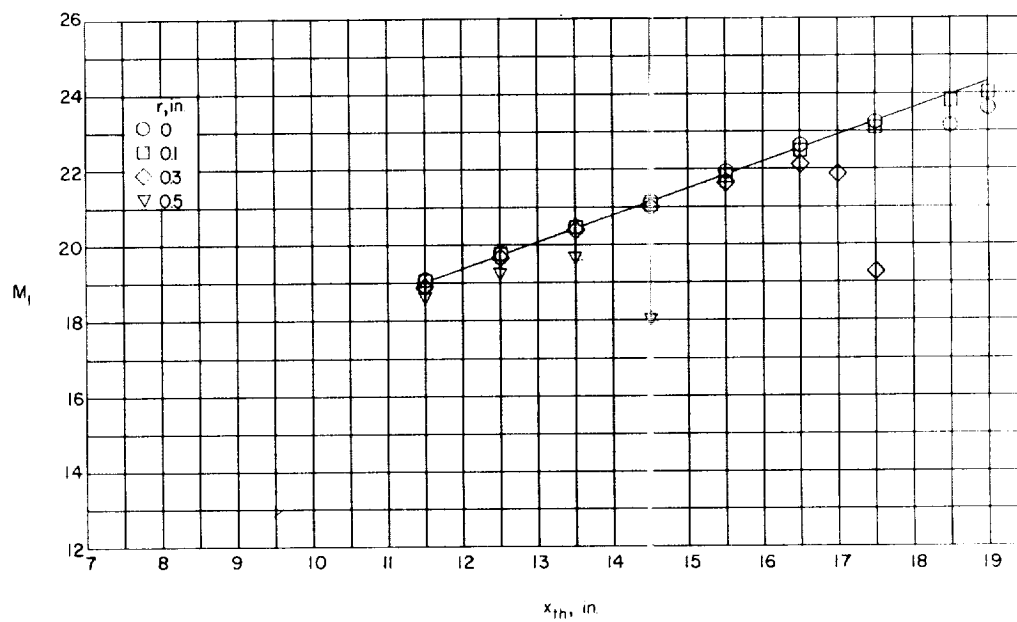
(d)   d* = 0.060 inch; $p_{t,1}$ = 2,015 lb/sq in. abs.

Figure 3.- Concluded.
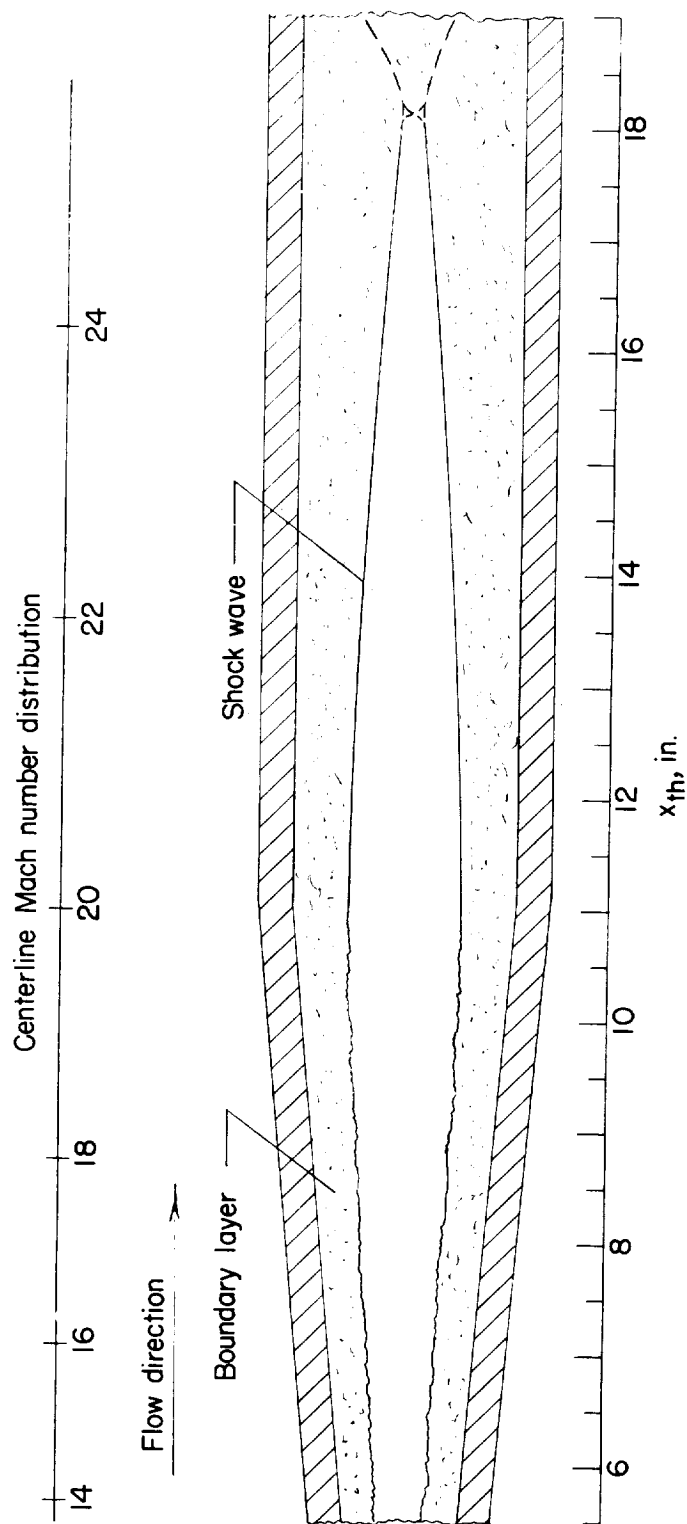
Figure 4.- Approximate test region in 2-inch helium tunnel. d* = 0.052 inch; $p_{t,1}$ = 2,015 lb/sq in. abs.
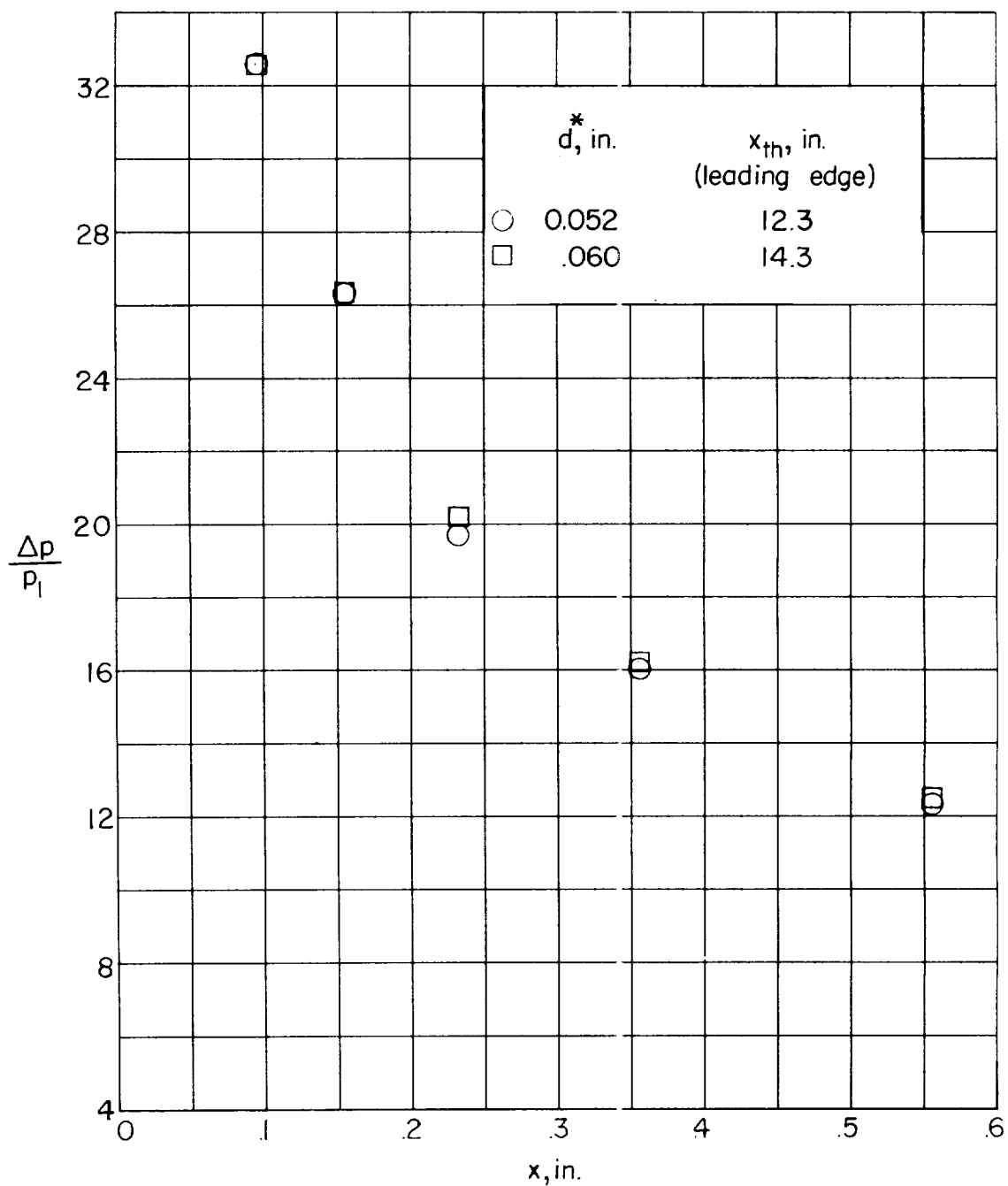
Figure 5.- Effect of nozzle throat on flat-plate pressures. M_1 = 21; $P_{t,1}$ = 2,015 lb/sq in. abs; w = 0.60 inch; t = 0.009 inch.
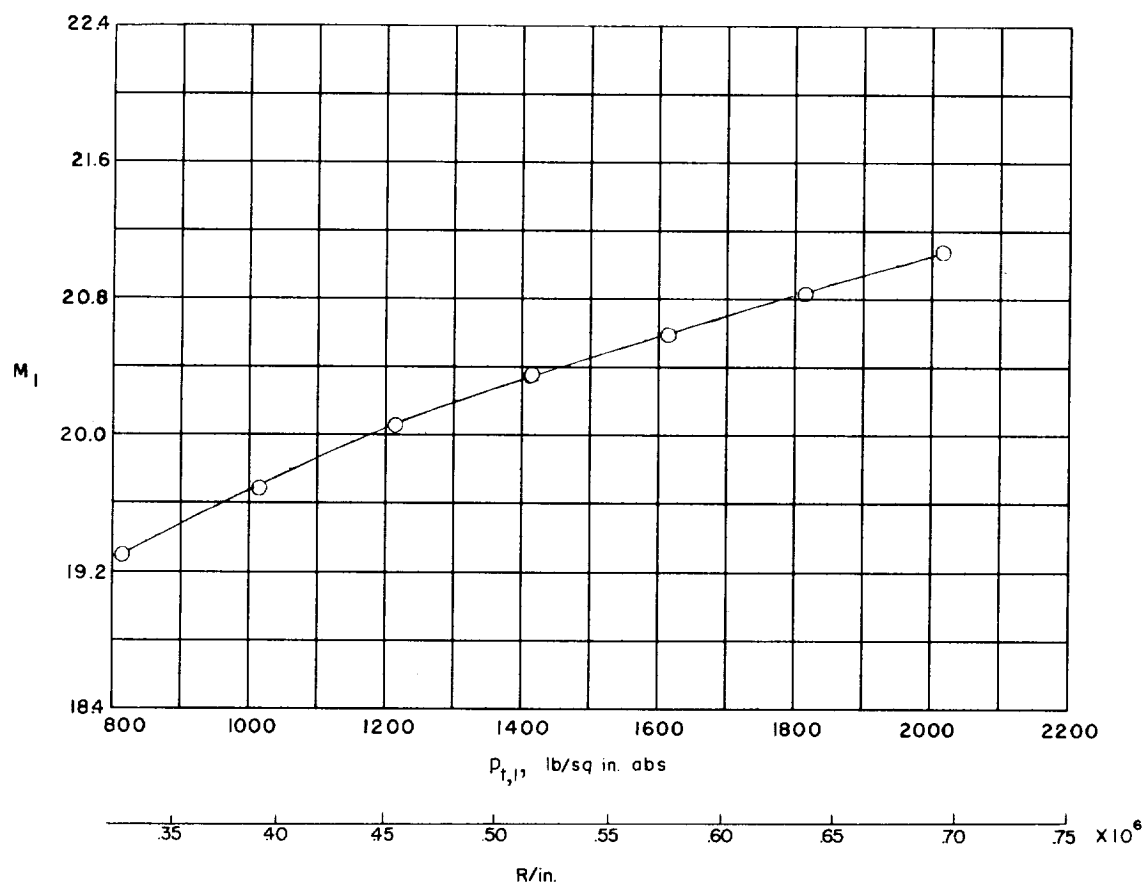
Figure 6.- Variation of Mach number with stagnation pressure at a
fixed station in the 2-inch helium tunnel. x_{th} = 14.5 inches;
d^* = 0.060 inch; probe 0.3 inch above tunnel center line.

$M_1 = 19$

$R_t = 806$
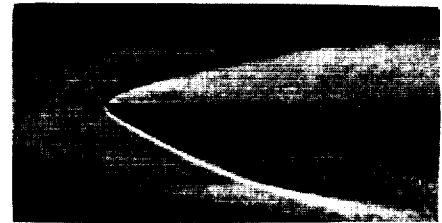
$R_t = 16,160$
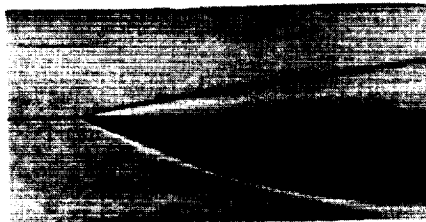
$M_1 = 21$

$R_t = 681$
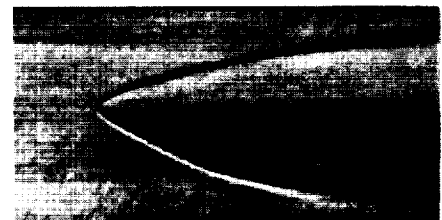
$R_t = 13,540$
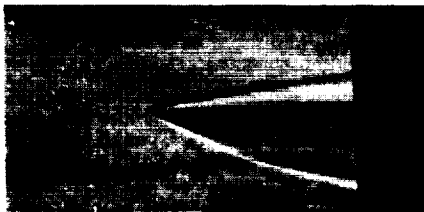
$M_1 = 23$

$R_t = 584$

$R_t = 11,680$

$t = 0.001$ in.

$t = 0.020$ in.

L-59-1850

Figure 7.- Schlieren photographs of flat-plate models.

$M_I = 19$

$R_t = 1612$

$R_t = 1612$

$M_I = 21$
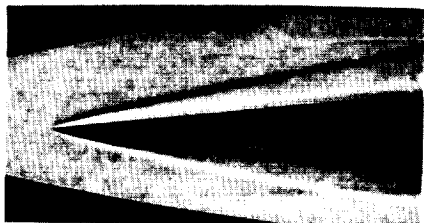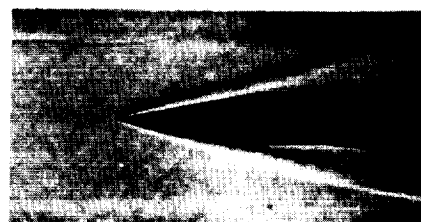
$R_t = 1362$

$R_t = 1362$

$M_I = 23$

$R_t = 1168$

$\theta = 5°$

$R_t = 1168$

$\theta = 10°$
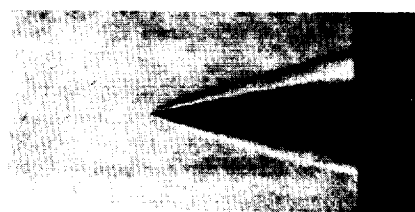
L-59-1851

Figure 8.- Schlieren photographs of wedge models. t = 0.002 inch.
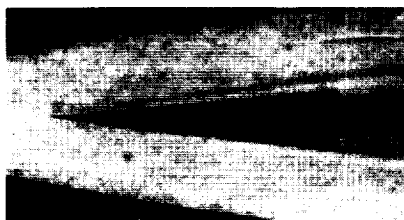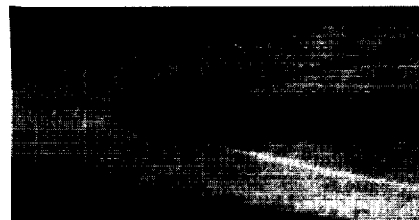
$M_1 = 19$

$R_d = 1612$ $R_d = 1612$
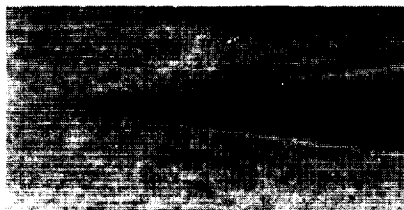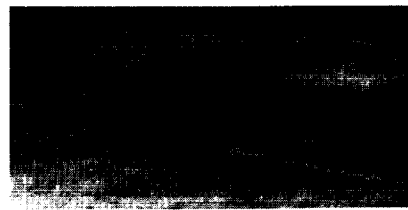
$M_1 = 21$

$R_d = 1362$ $R_d = 1362$
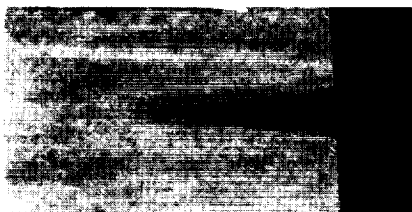
$M_1 = 23$

$R_d = 1168$ $R_d = 1168$

$\theta = 5°$ $\theta = 10°$

(a) d = 0.002 inch.   L-59-1852

Figure 9.- Schlieren photographs of cone models.

$M_l = 19$

$R_d = 48,360$

$R_d = 48,360$

$M_l = 21$

$R_d = 40,860$

$R_d = 40,860$

$M_l = 23$
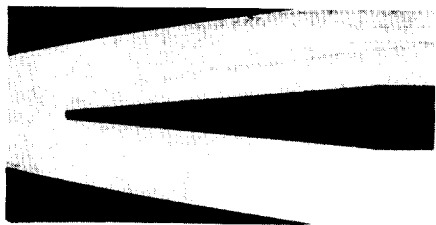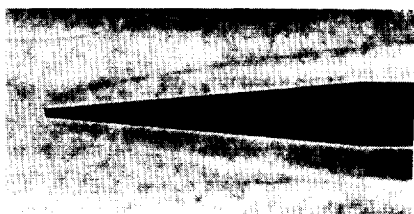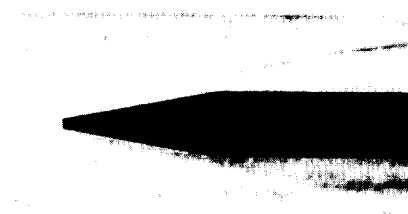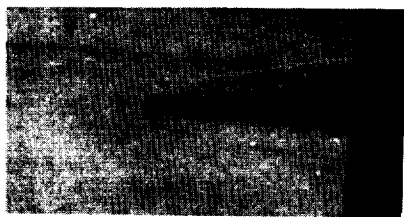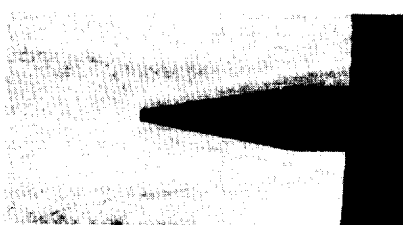
$R_d = 35,040$

$R_d = 35,040$

$\theta = 5°$

$\theta = 10°$

(b) d = 0.060 inch.

L-59-1853

Figure 9.- Concluded.
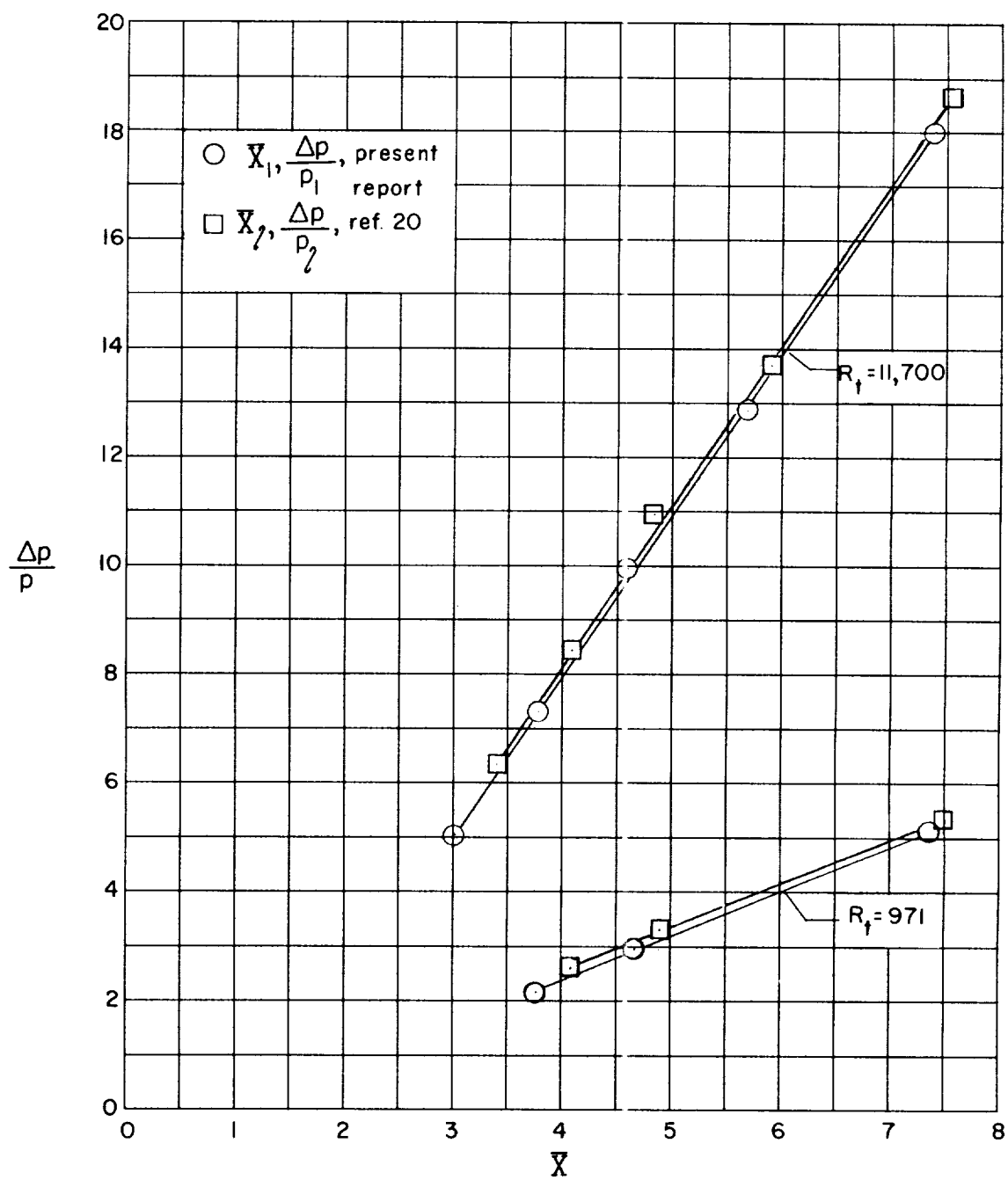
(a) $M_1 = 1''$.

Figure 10.- Comparison of two methods of handling flat-plate pressure-
distribution data when obtained in the presence of a free-stream
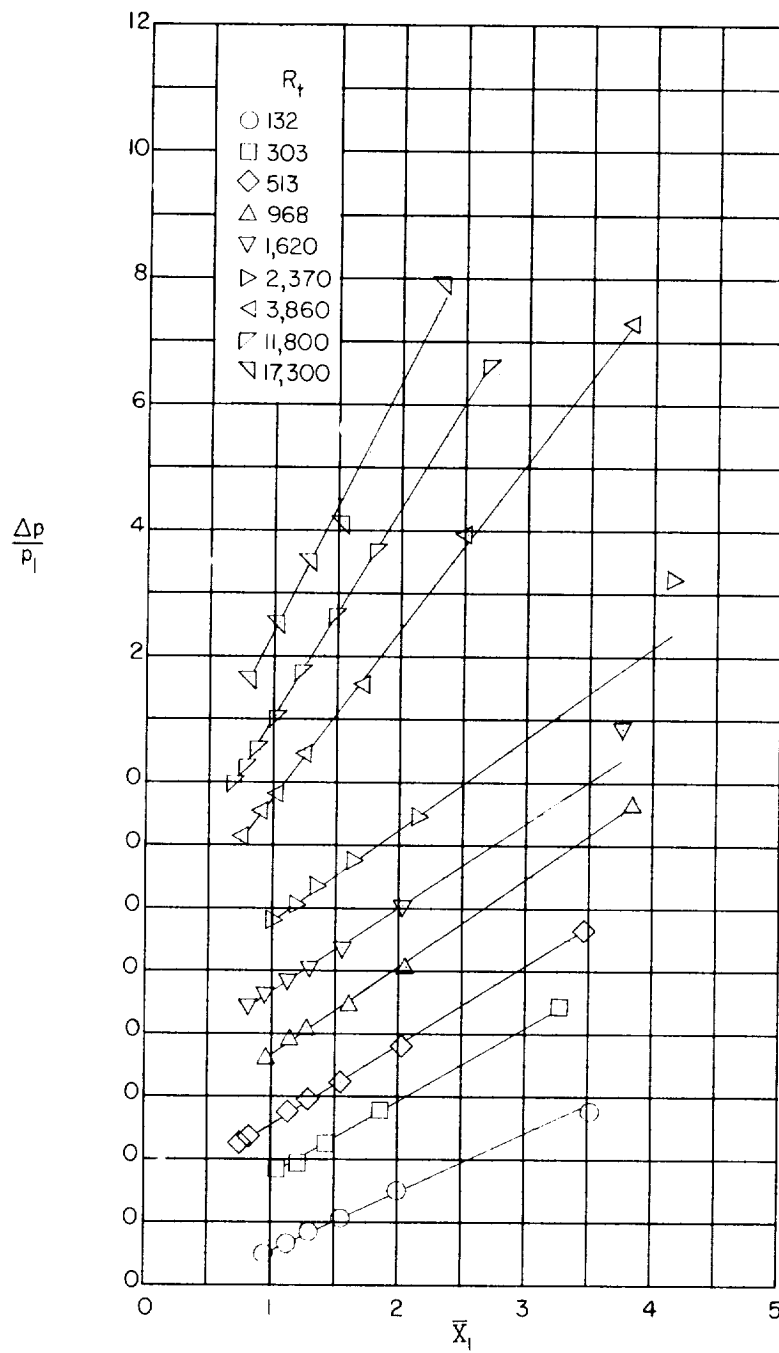Mach number gradient.
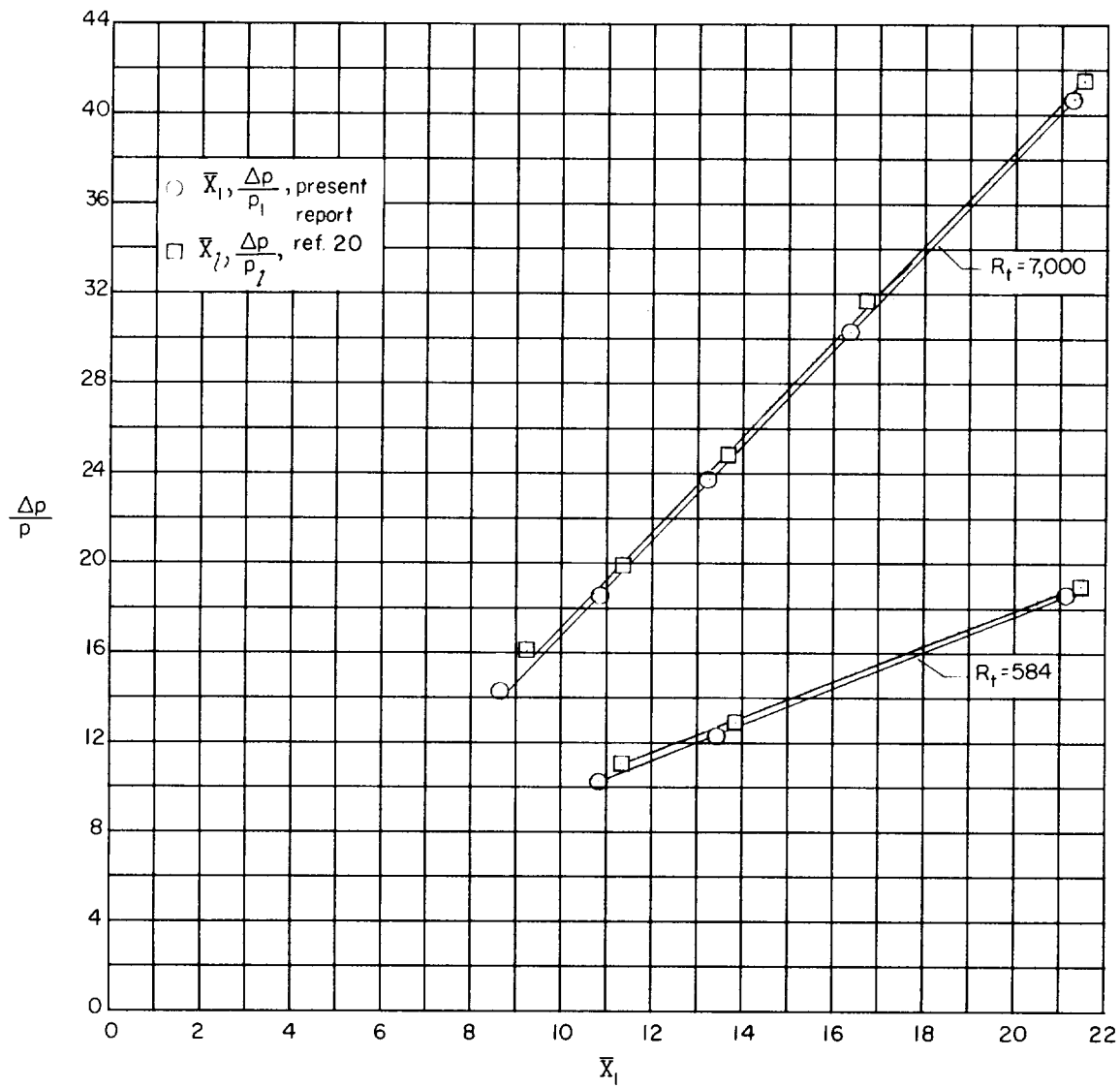
(b) $M_1 = 23$.

Figure 10.- Concluded.
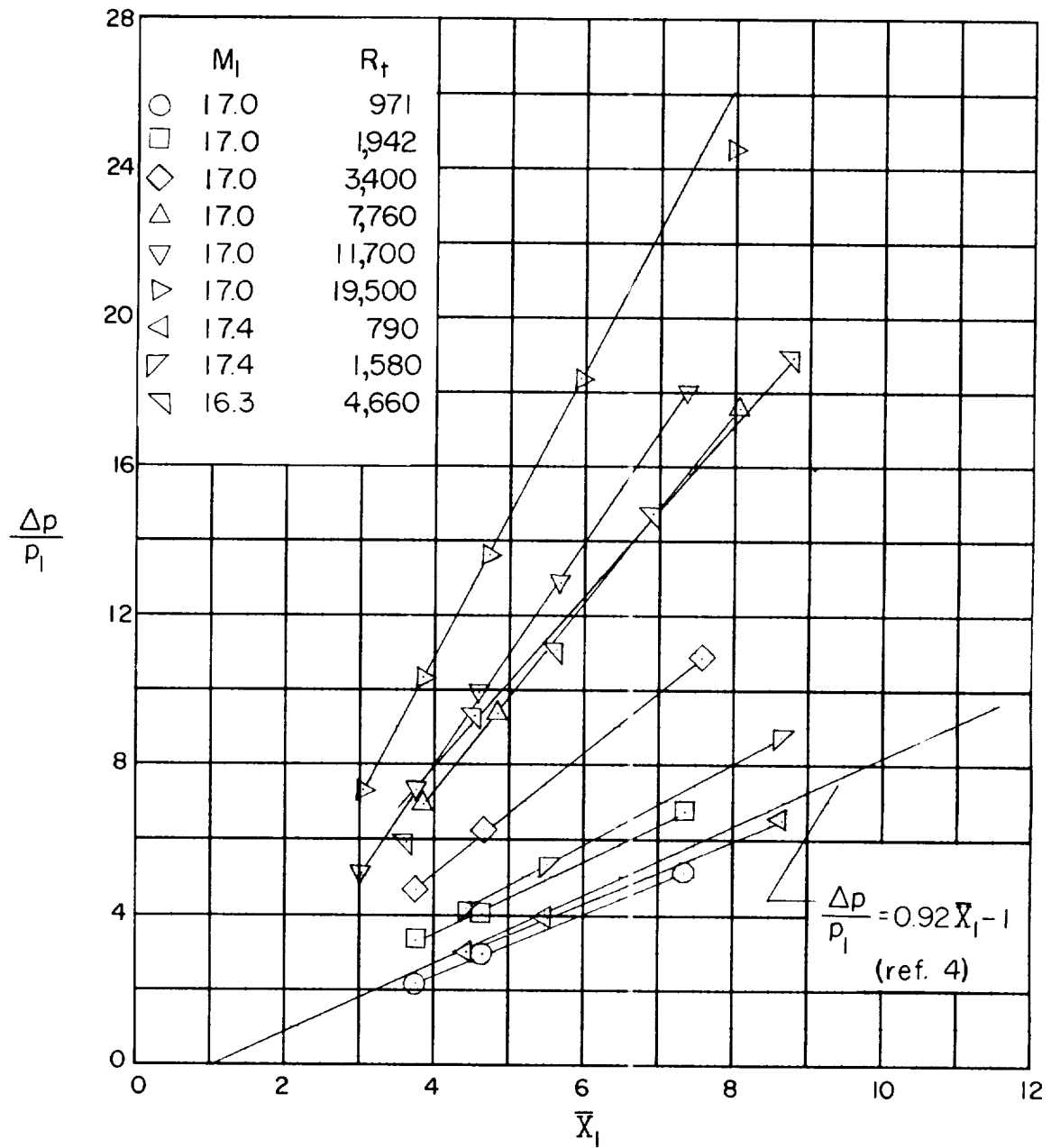
(a) $M_1 \approx 17$.

Figure 11.- Variation of the induced static-pressure ratio on flat plates with the hypersonic viscous-interaction parameter $\overline{X}_1$. w = 0.8 inch.
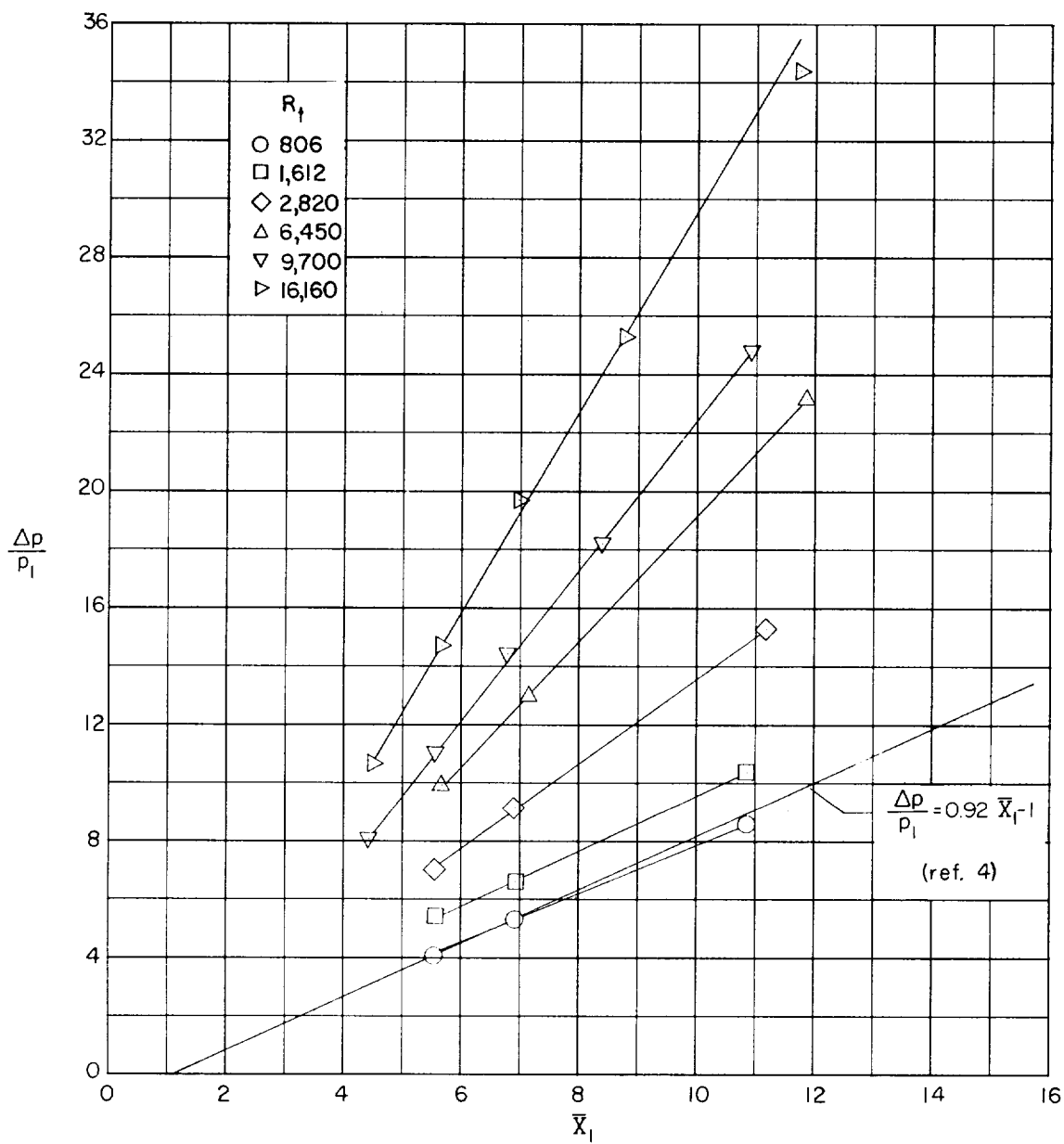
(b) $M_1 = 19$.

Figure 11.- Continued.
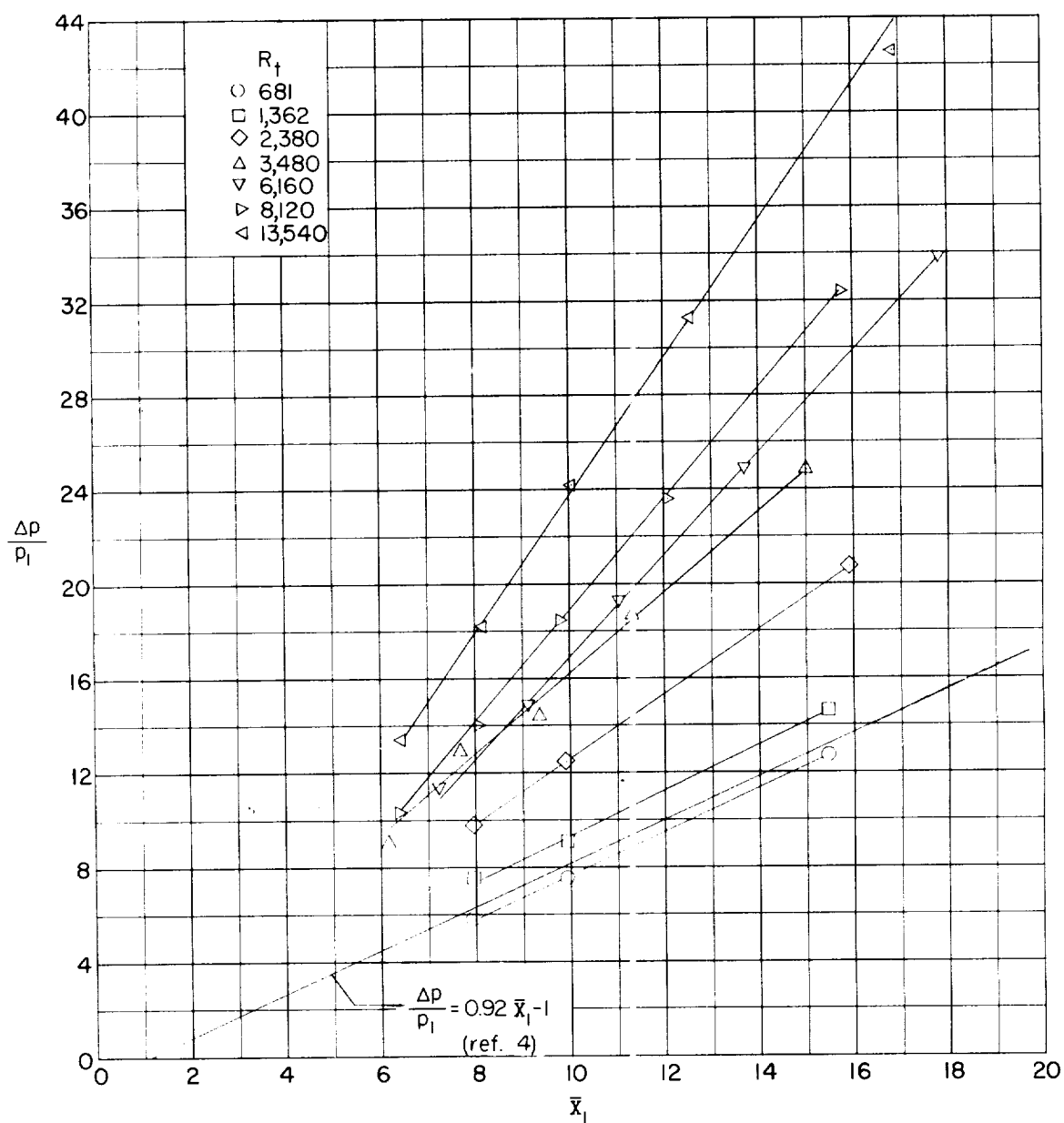
(c) $M_1 = 21$.

Figure 11.- Continued.
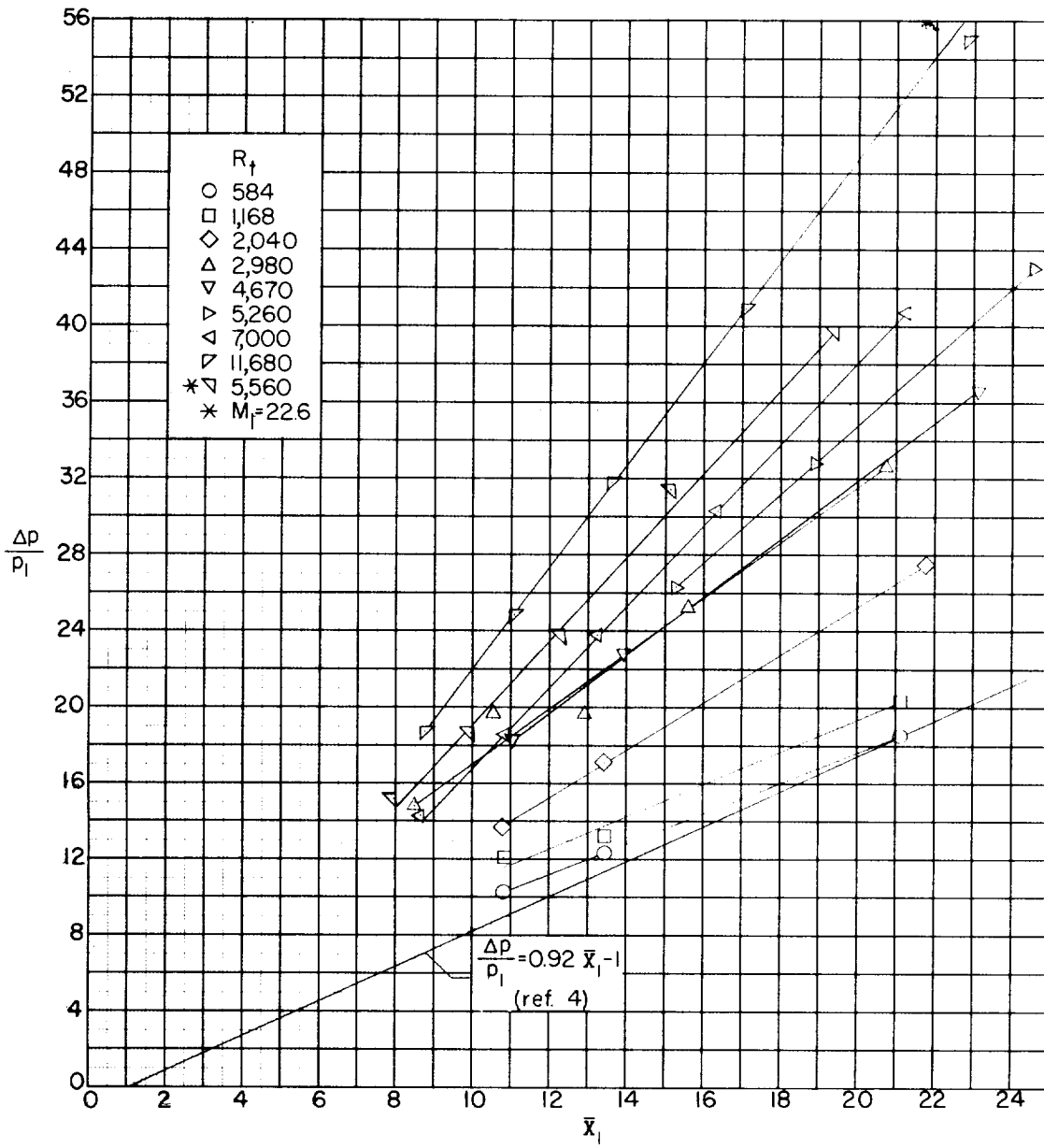
(d) $M_1 = 23$.

Figure 11.- Concluded.
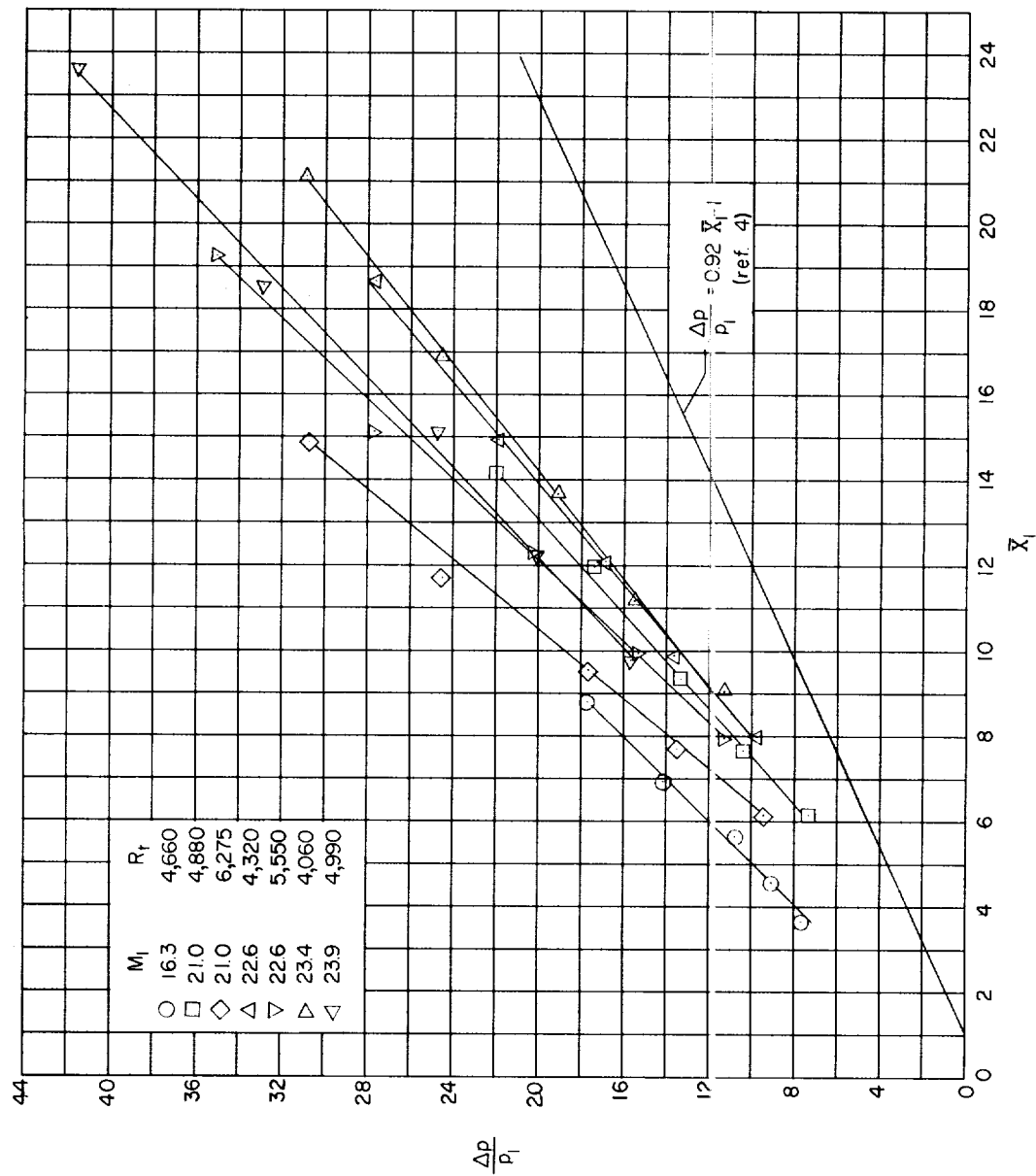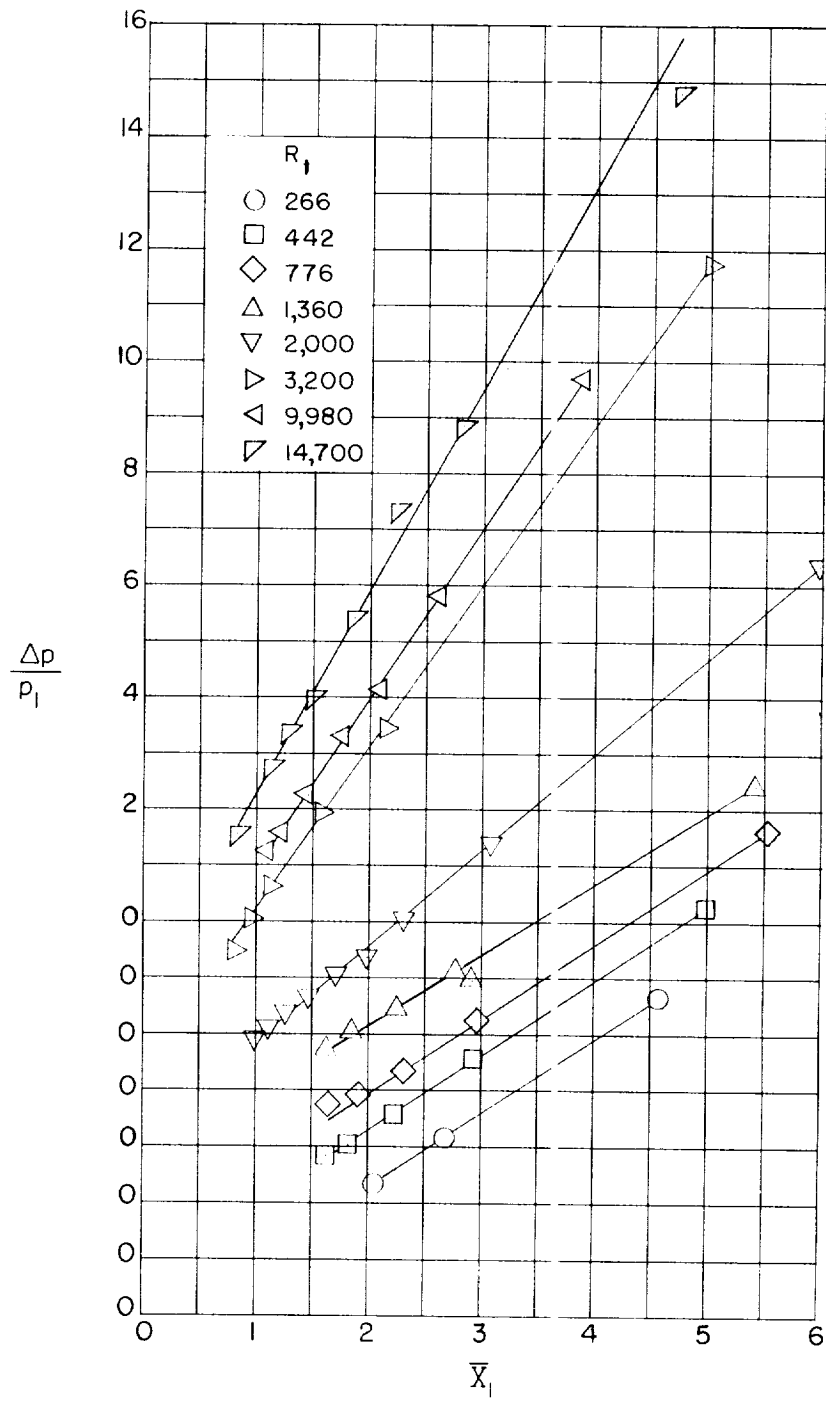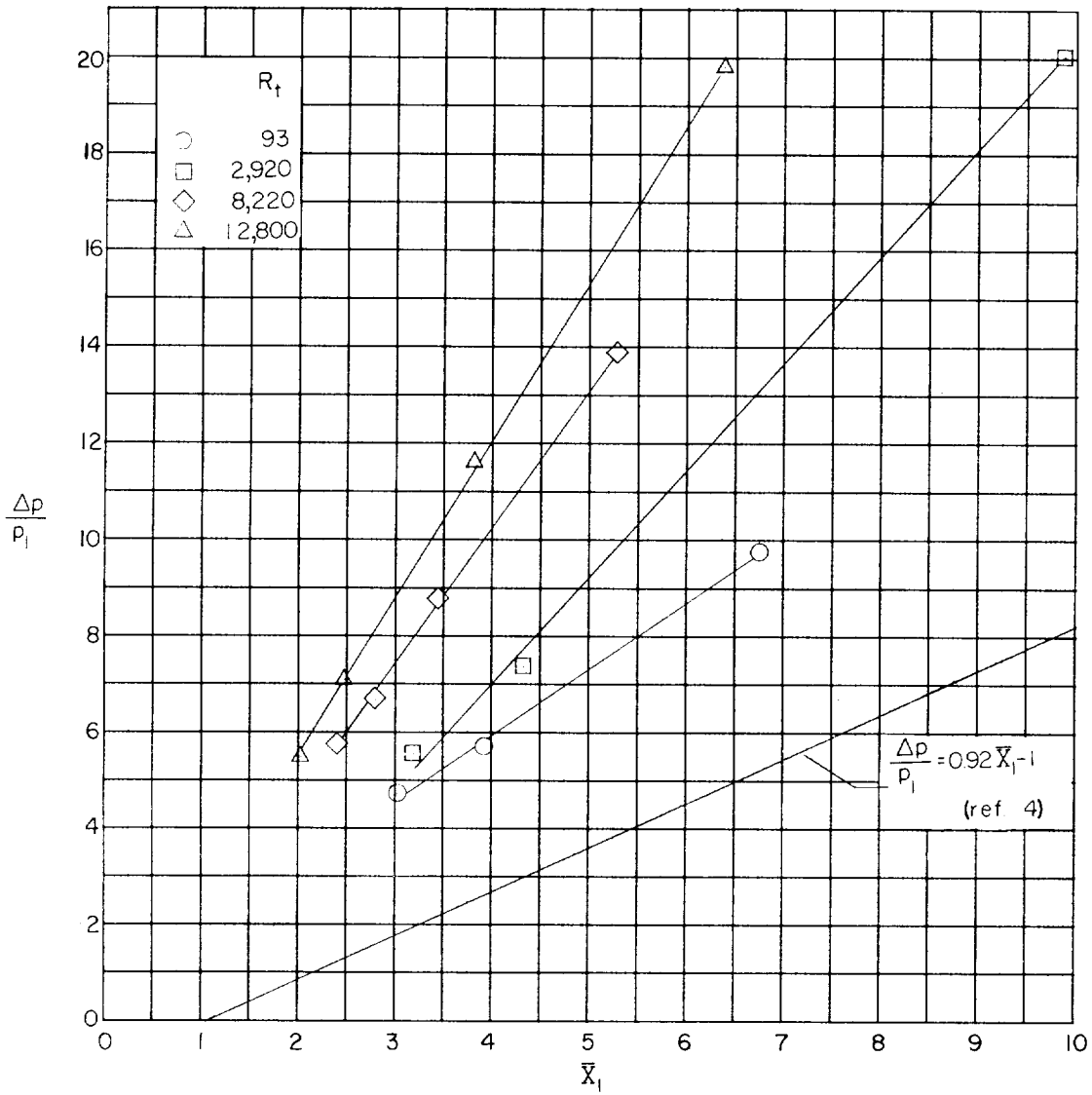
Figure 12.- Variation of the induced static-pressure ratio on flat plates with the hypersonic viscous-interaction parameter $\bar{X}_1$. $w = 0.6$ inch.
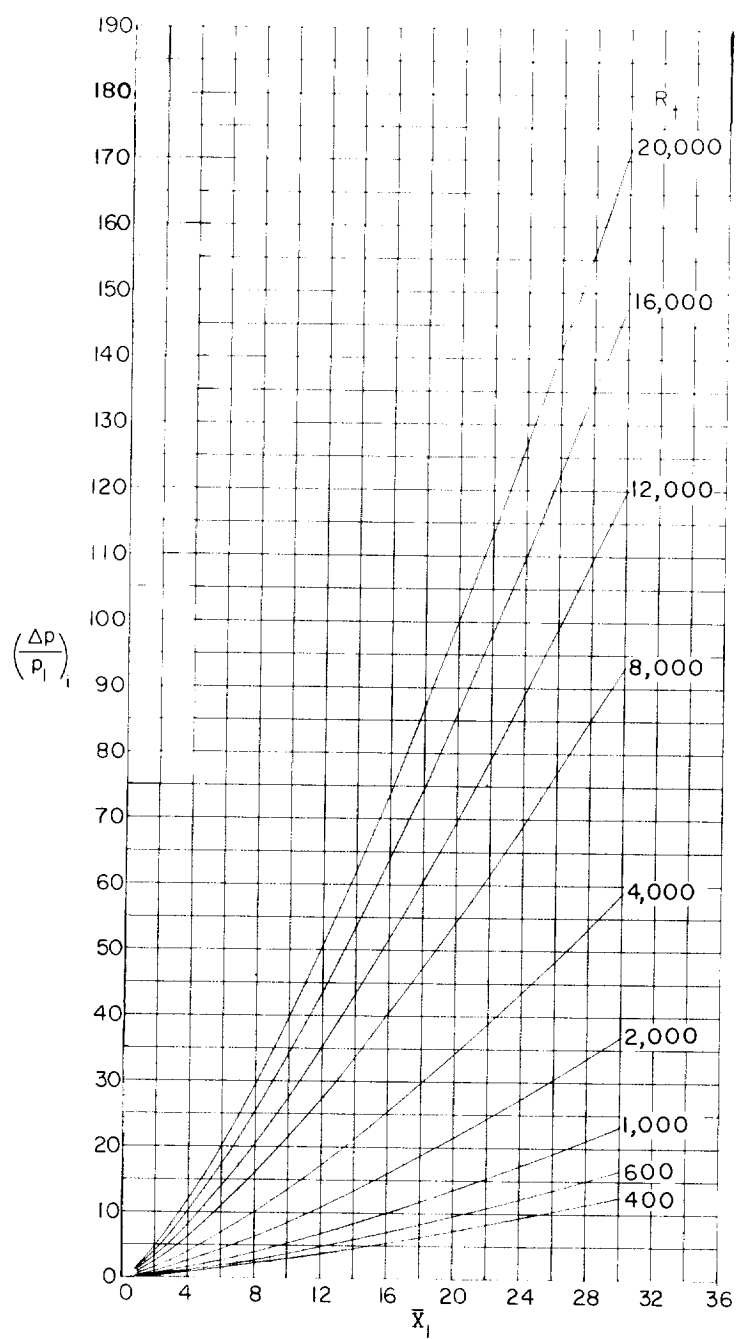
(a) $M_1 = 17$.

Figure 13.- Variation of blast-wave prediction of induced static-pressure
ratio with $\overline{X}$ for various values of R_t.
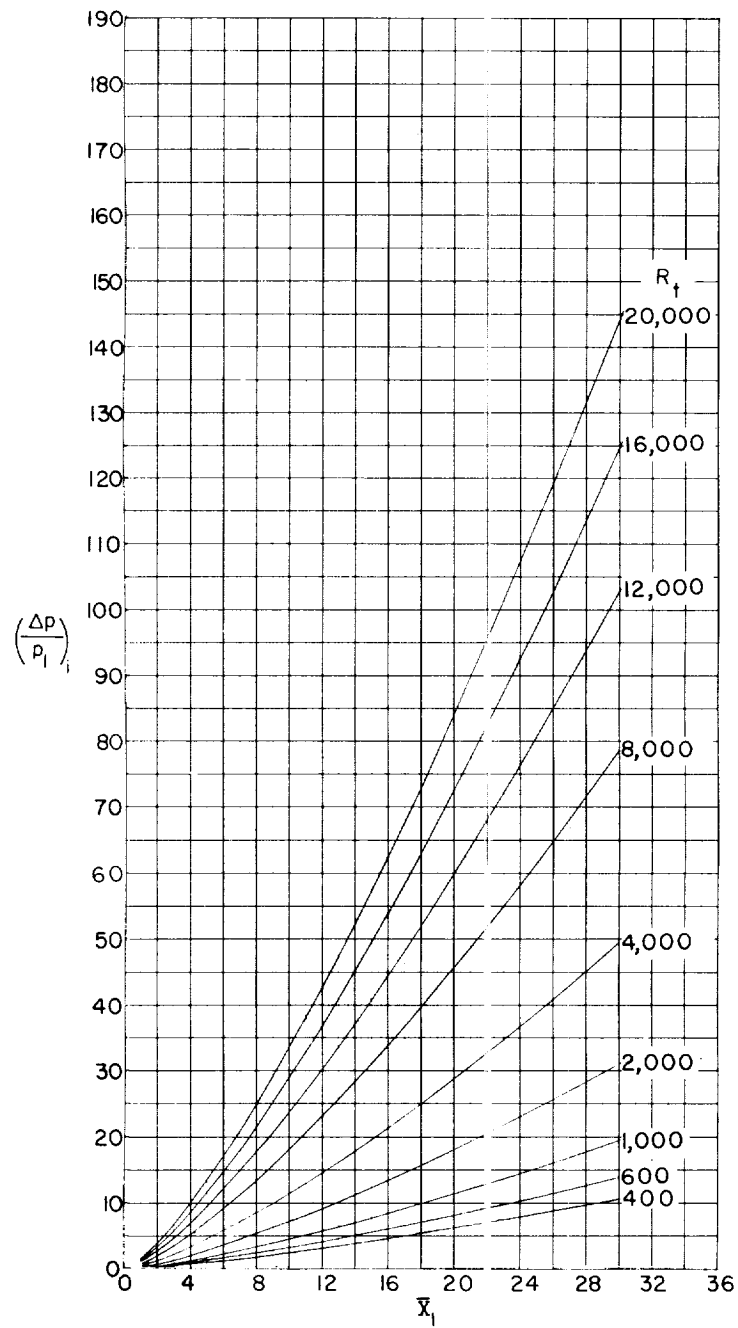
(b) $M_1 = 1.9$.

Figure 13.- Continued.
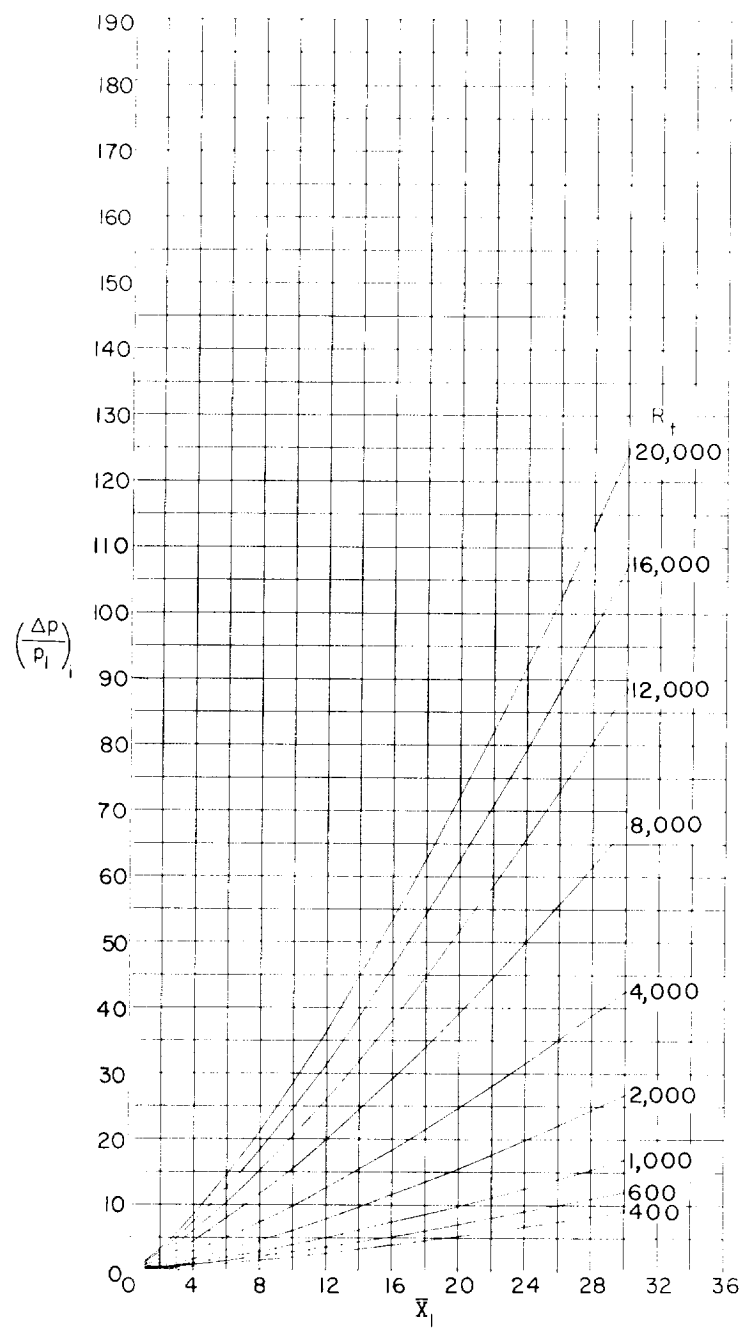
(c) $M_1 = 21$.

Figure 13.- Continued.
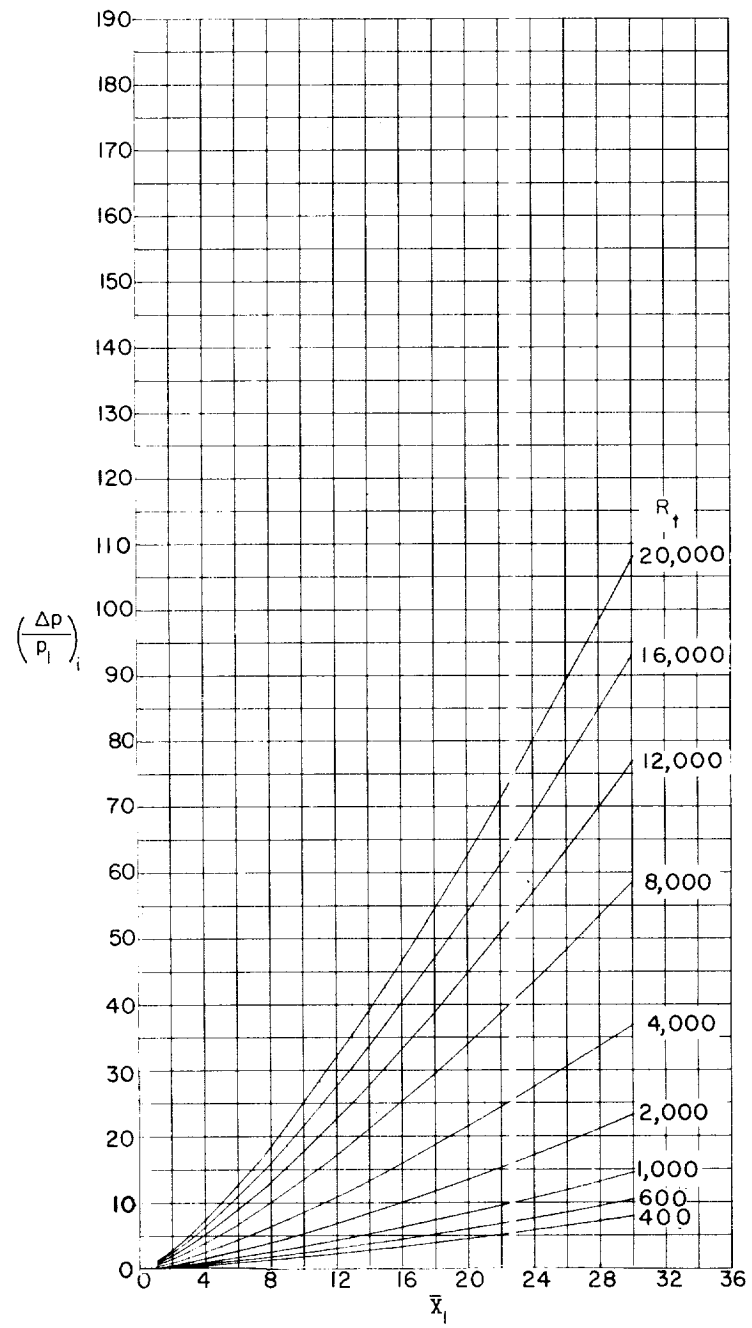
(d) $M_1 = 23$.

Figure 13.- Concluded.
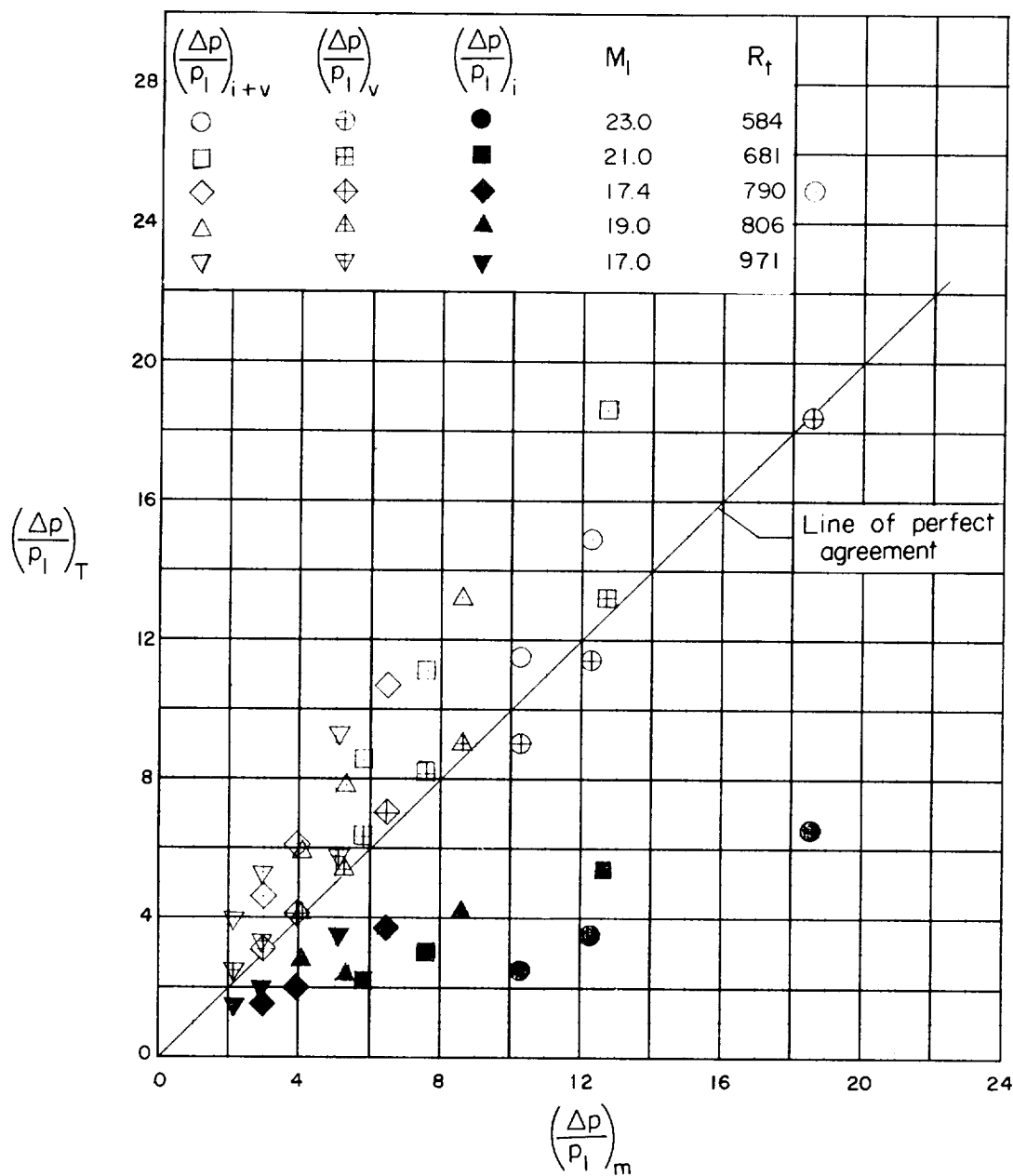
(a) $0 < R_t < 1,000$.

Figure 14.- Variation of viscous theory $\left(\dfrac{\Delta p}{p_1}\right)_v$, inviscid theory $\left(\dfrac{\Delta p}{p_1}\right)_i$, and the linear addition of viscous and inviscid theories $\left(\dfrac{\Delta p}{p_1}\right)_{i+v}$ with $\left(\dfrac{\Delta p}{p_1}\right)_m$ for various values of M_1 and R_t.

$\left(\dfrac{\Delta p}{p_l}\right)_{i+v}$	$\left(\dfrac{\Delta p}{p_l}\right)_{v}$	$\left(\dfrac{\Delta p}{p_l}\right)_{i}$	M_l	R_t
◯	⊕	●	23.0	1,168
▢	⊞	■	21.0	1,362
◇	⬦	◆	17.4	1,580
△	◮	▲	19.0	1,612
▽	▼	▼	17.0	1,942

Line of perfect agreement

$\left(\dfrac{\Delta p}{p_l}\right)_T$

$\left(\dfrac{\Delta p}{p_l}\right)_m$
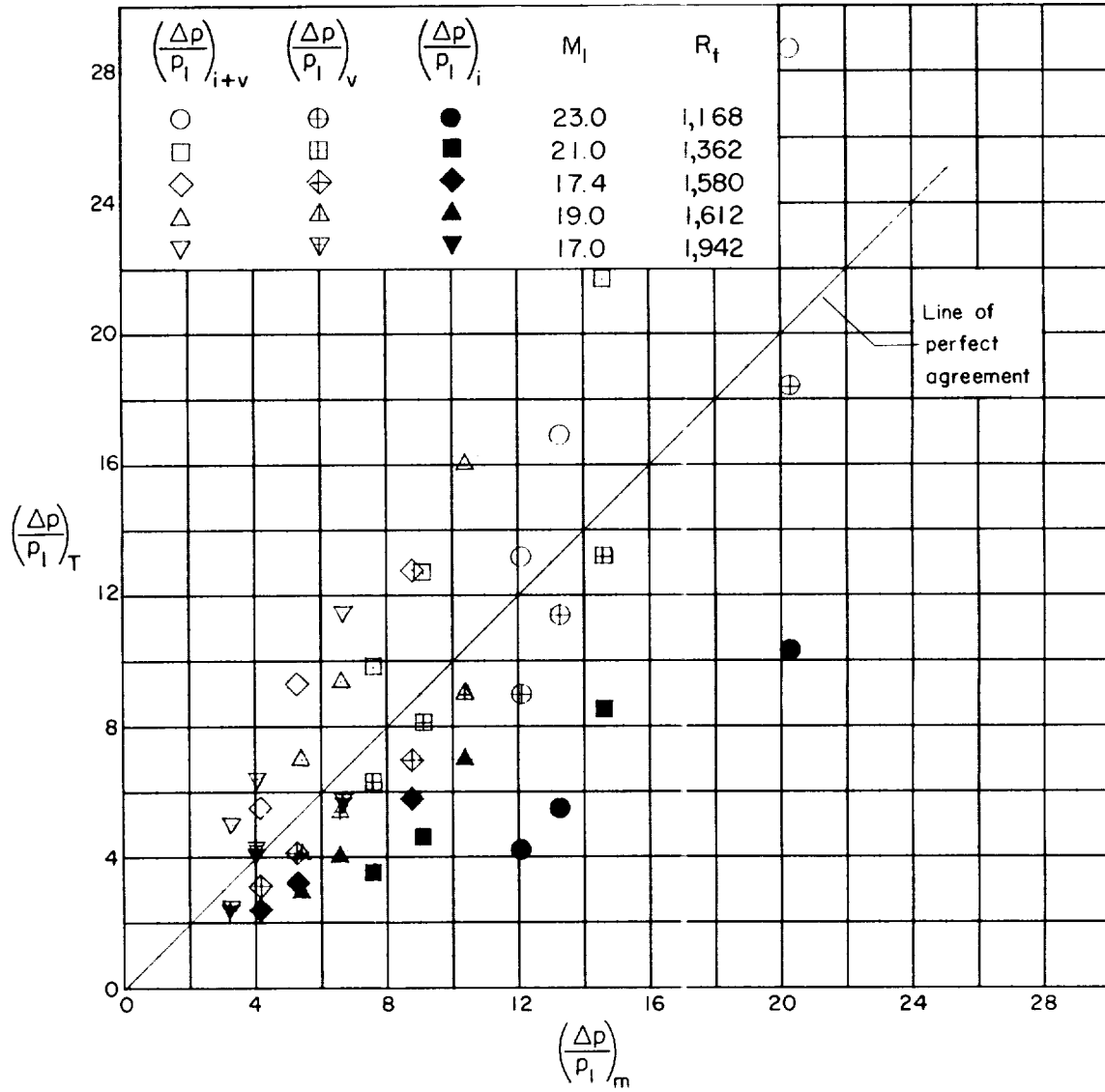
(b) $1,000 < R_t < 2,000.$

Figure 14.- Continued.
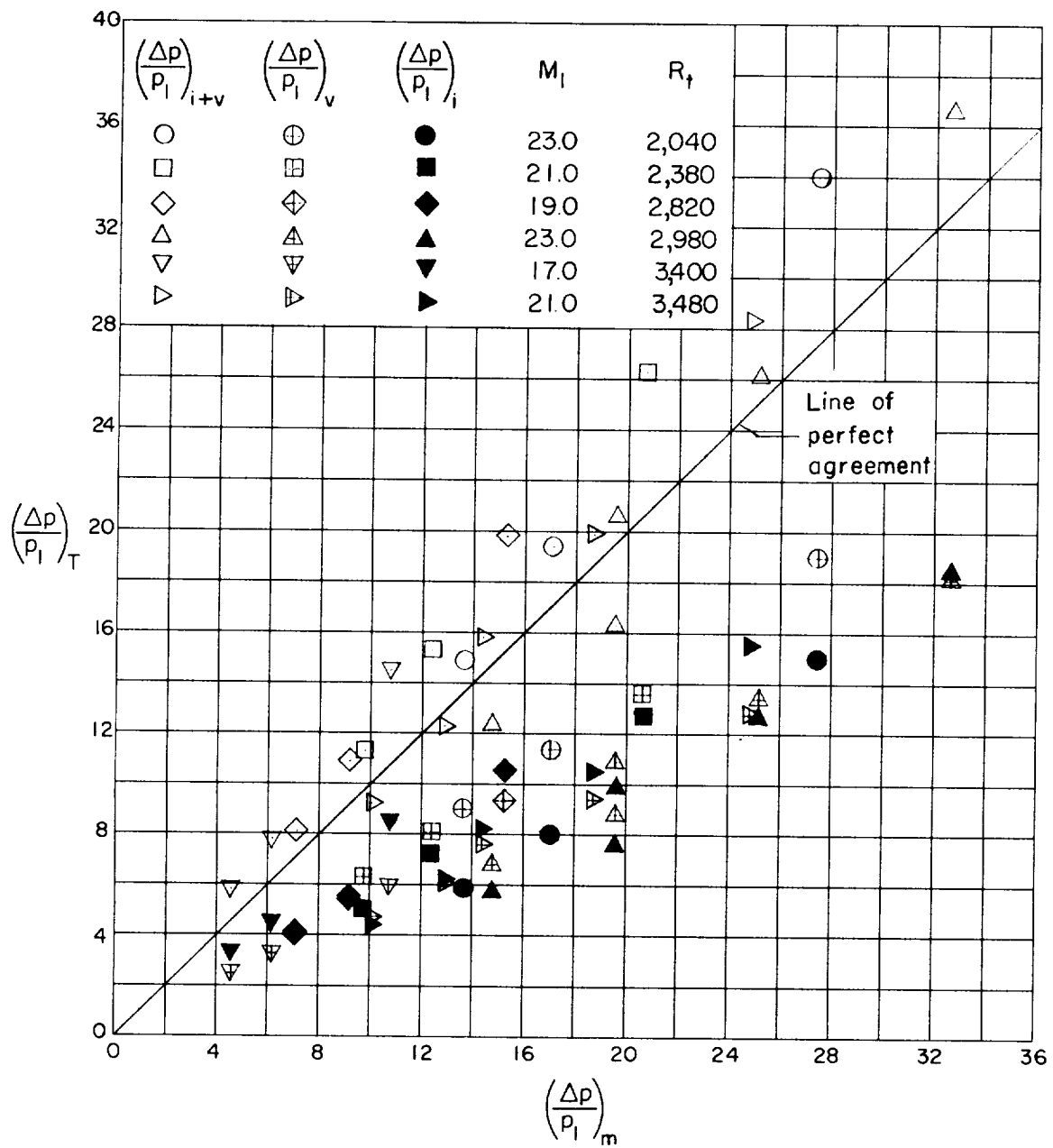
(c) $2,000 < R_t < 4,000$.

Figure 14.- Continued.
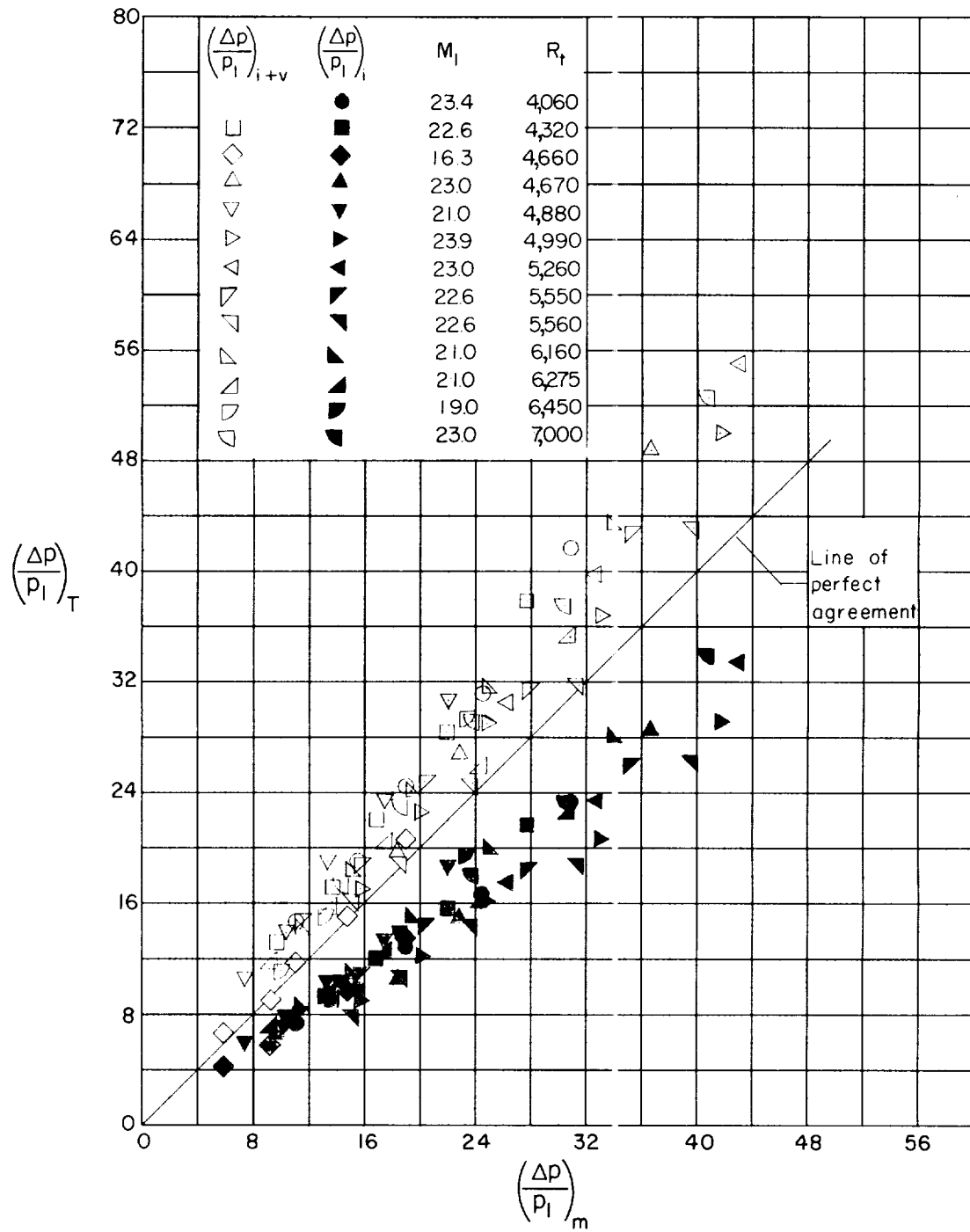
(d) 4,000 < R_t < 7,000.

Figure 14.- Continued.
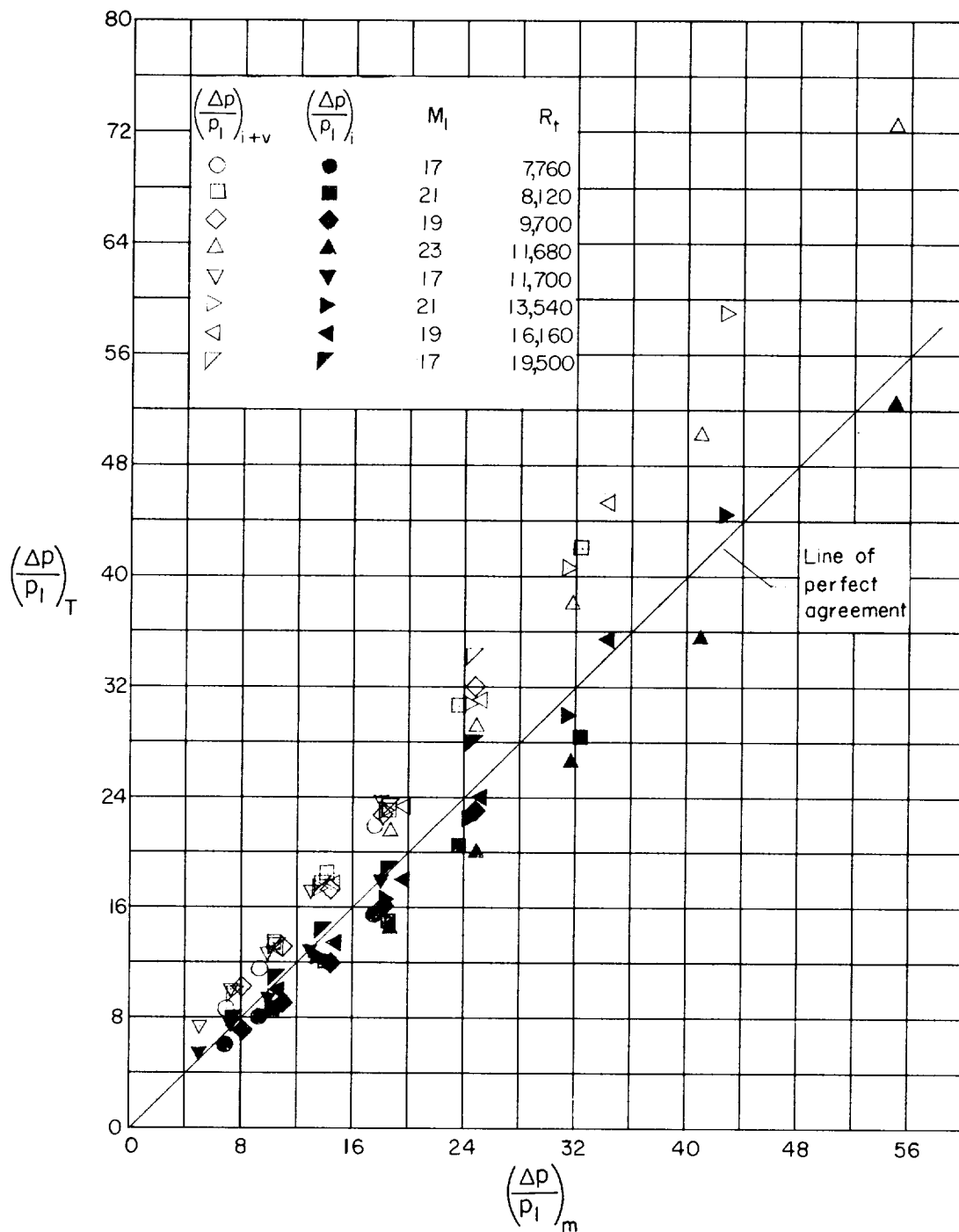
(e) $7,000 < R_t < 20,000$.

Figure 14.- Concluded.
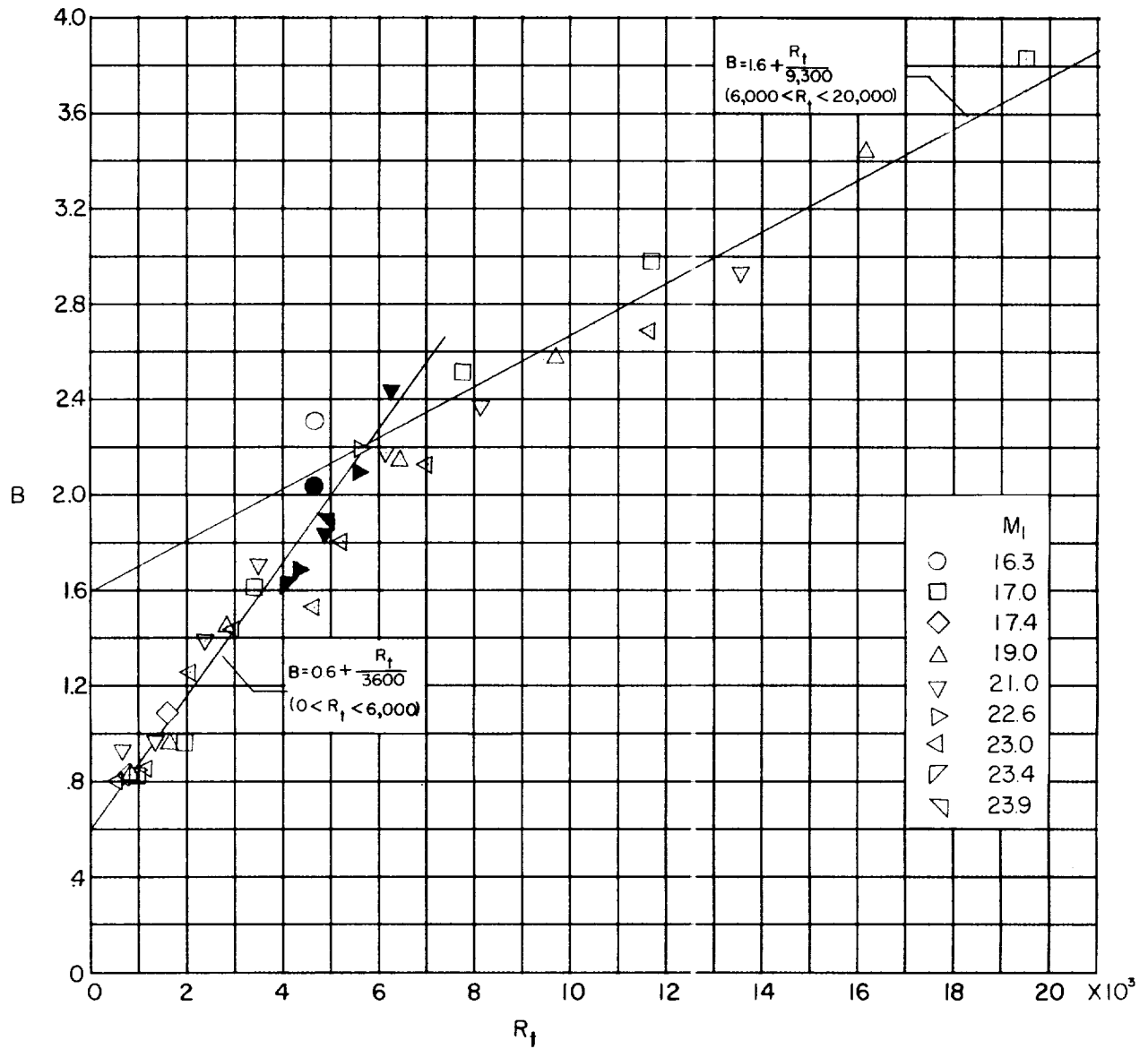
Figure 15.- Variation of the slopes of the induced static-pressure-
ratio curves $B = \dfrac{d}{d\bar{x}_1}\left(\dfrac{\Delta p}{p_1}\right)$ from figures 11 and 12, with R_t. Open
symbols are for $w = 0.8$ inch and solid symbols are for $w = 0.6$ inch.

(a) $M_1 = 11.4$.

Figure 16.- Variation of the induced static-pressure ratio on flat
plates with the hypersonic viscous-interaction parameter $\overline{X}_1$. Data
taken from reference 18.

(b) $M_1 = 12.7$.

Figure 16.- Continued.

(c) $M_1 = 13.8$.

Figure 16.- Concluded.
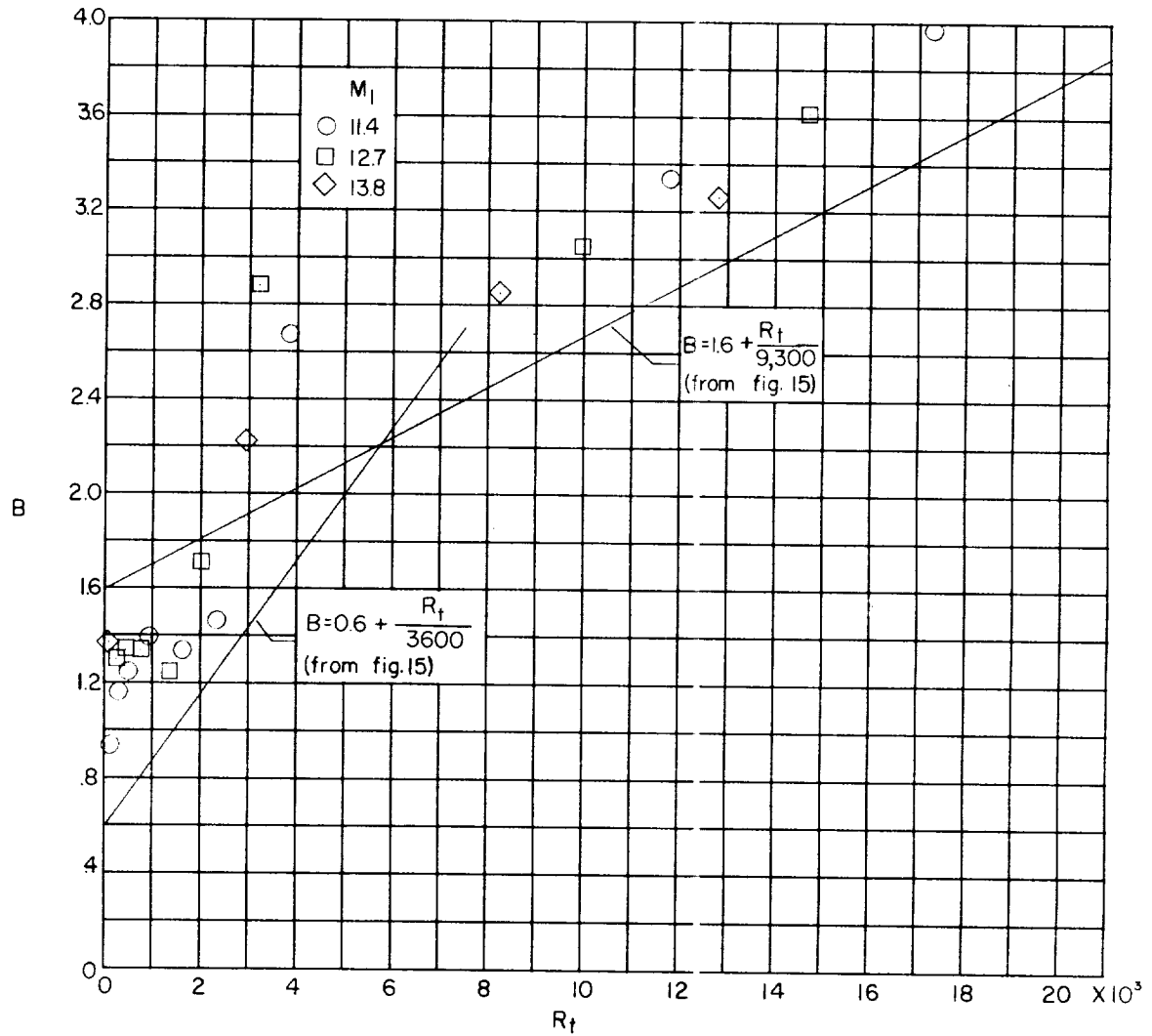
Figure 17.- Variation of the slopes of the induced static-pressure-ratio curves $B = \dfrac{d}{d\bar{x}_1}\left(\dfrac{\Delta p}{p_1}\right)$ from figure 16, with R_t .
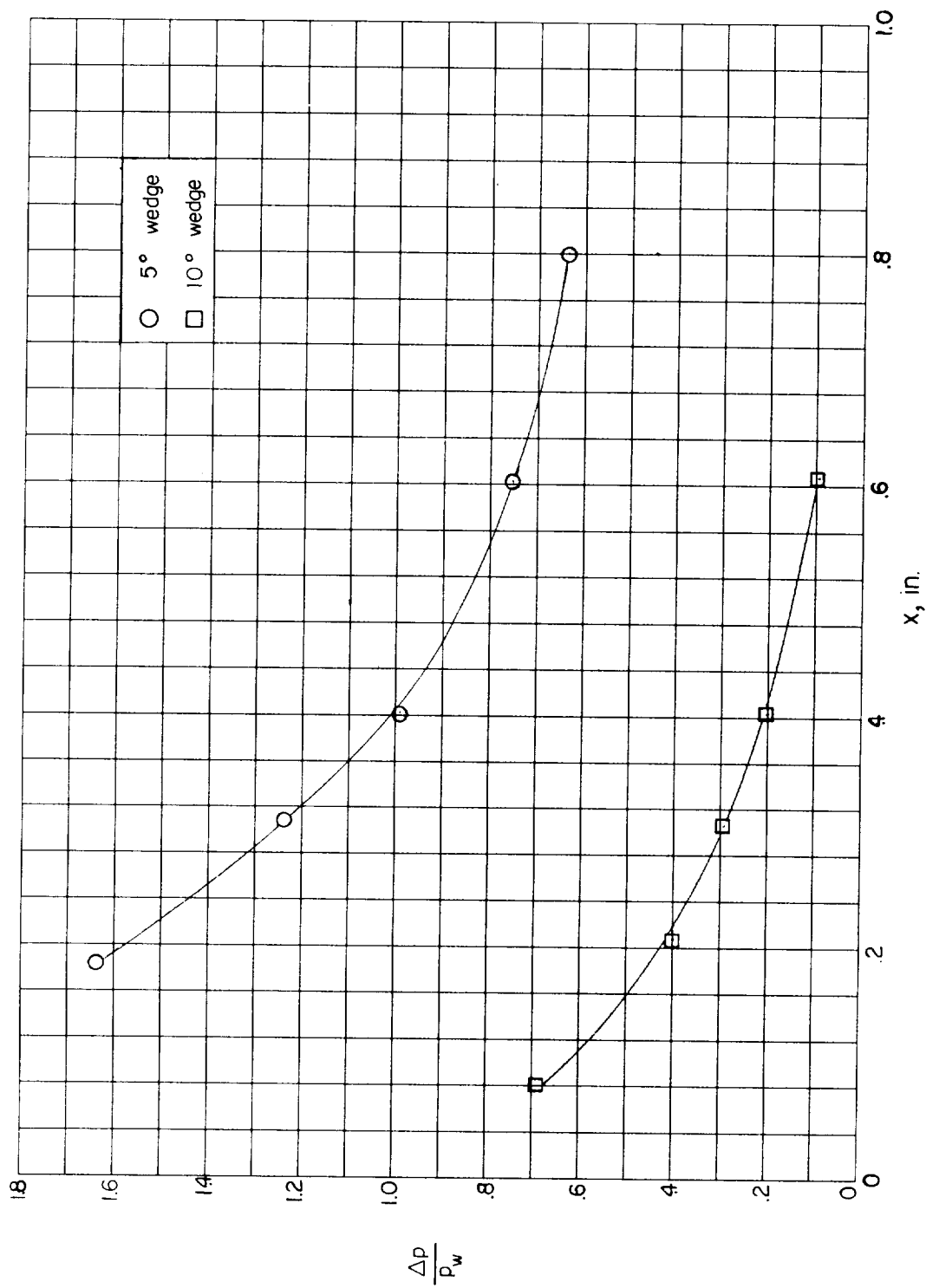
Figure 18.- Variation of the induced static-pressure ratio with distance from the leading edge of the 5° and 10° wedges. $M_l = 21$; $R_t = 1,360$.
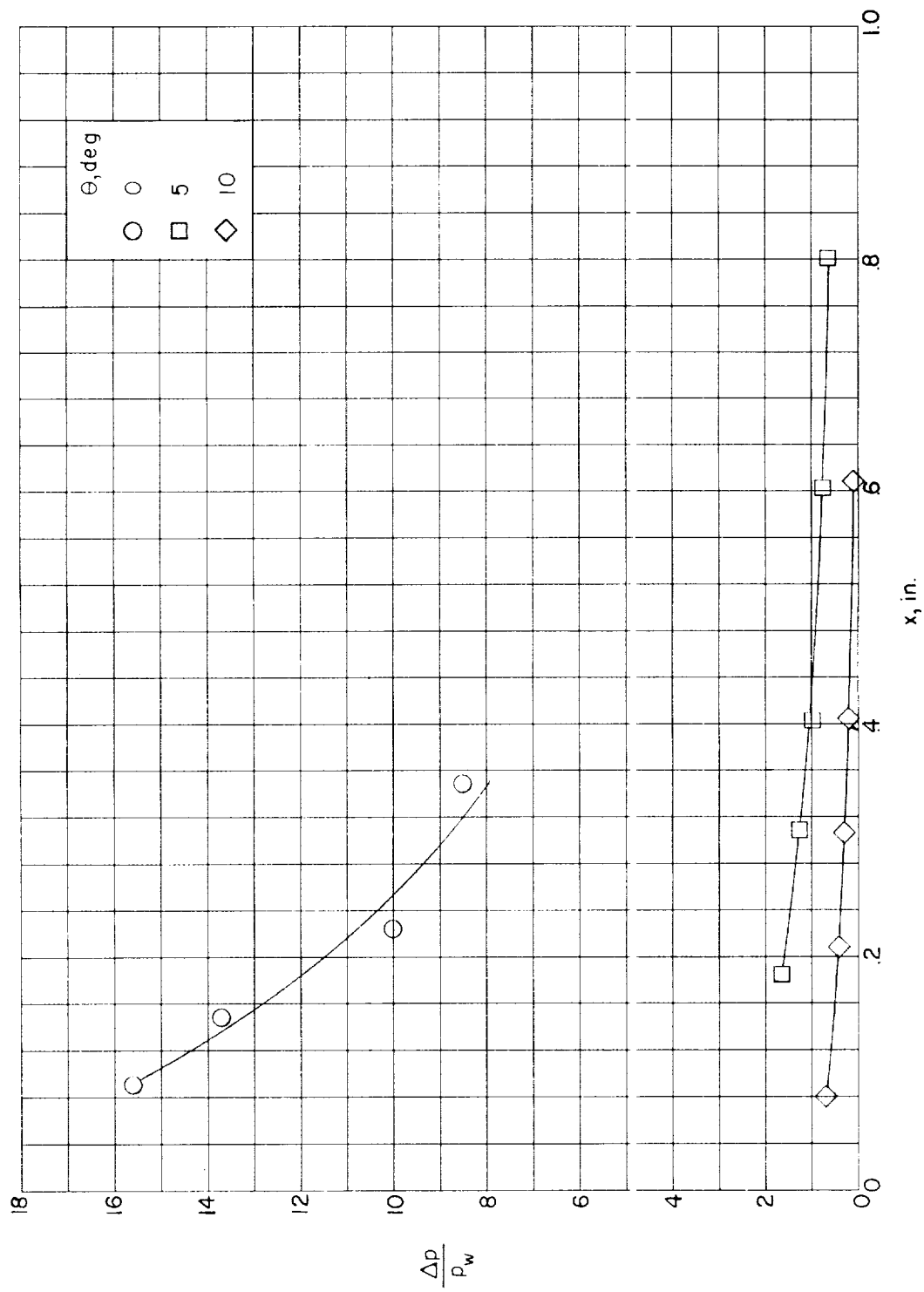
Figure 19.- Illustration of decreased dependence of pressure distribution on boundary layer with increasing flow-deflection angle. $M_1 = 21$; $R_t = 1,360$.
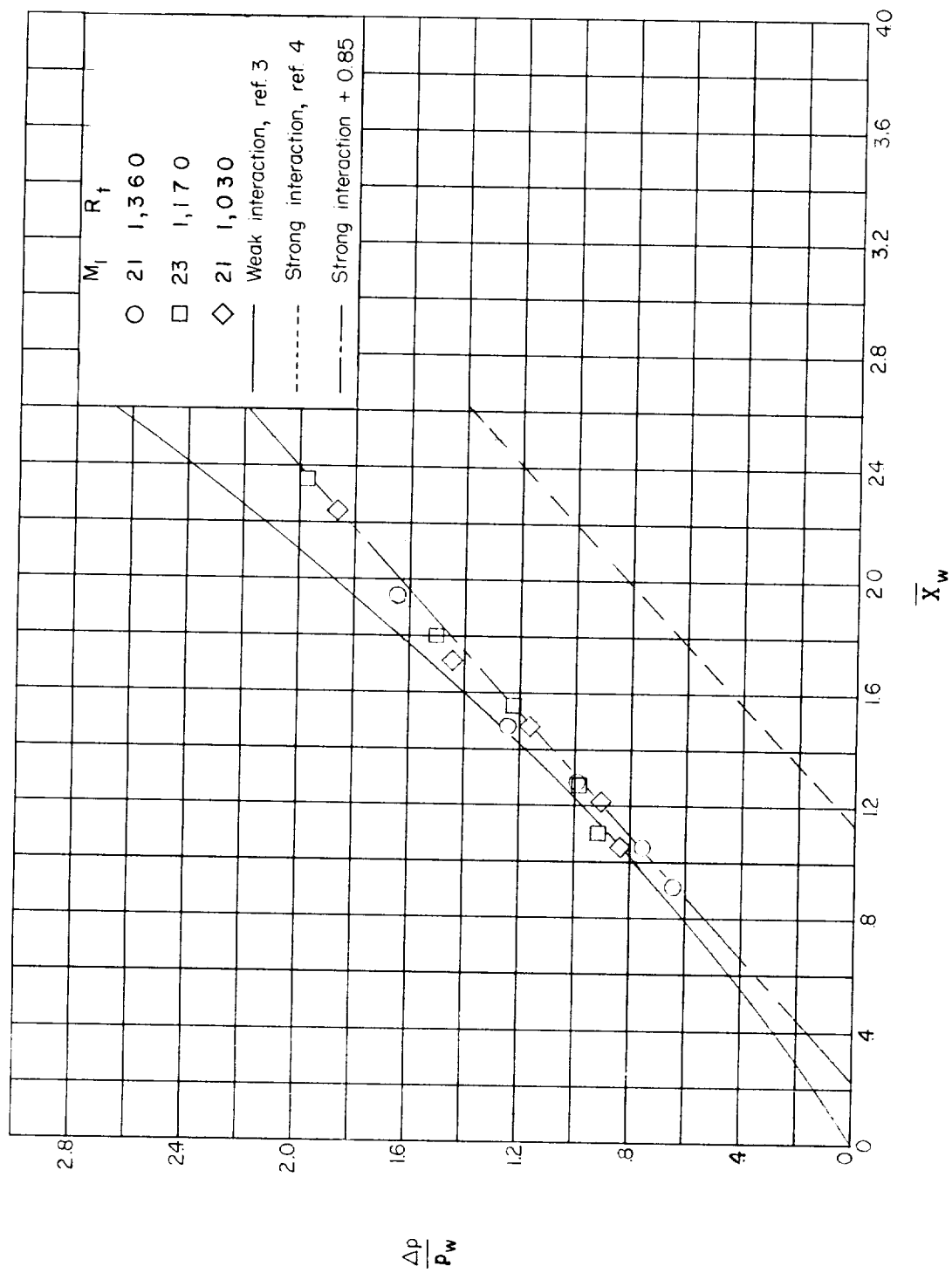
Figure 20.- Variation of the induced static-pressure ratio with $\overline{X}_w$ for the 5° wedge.
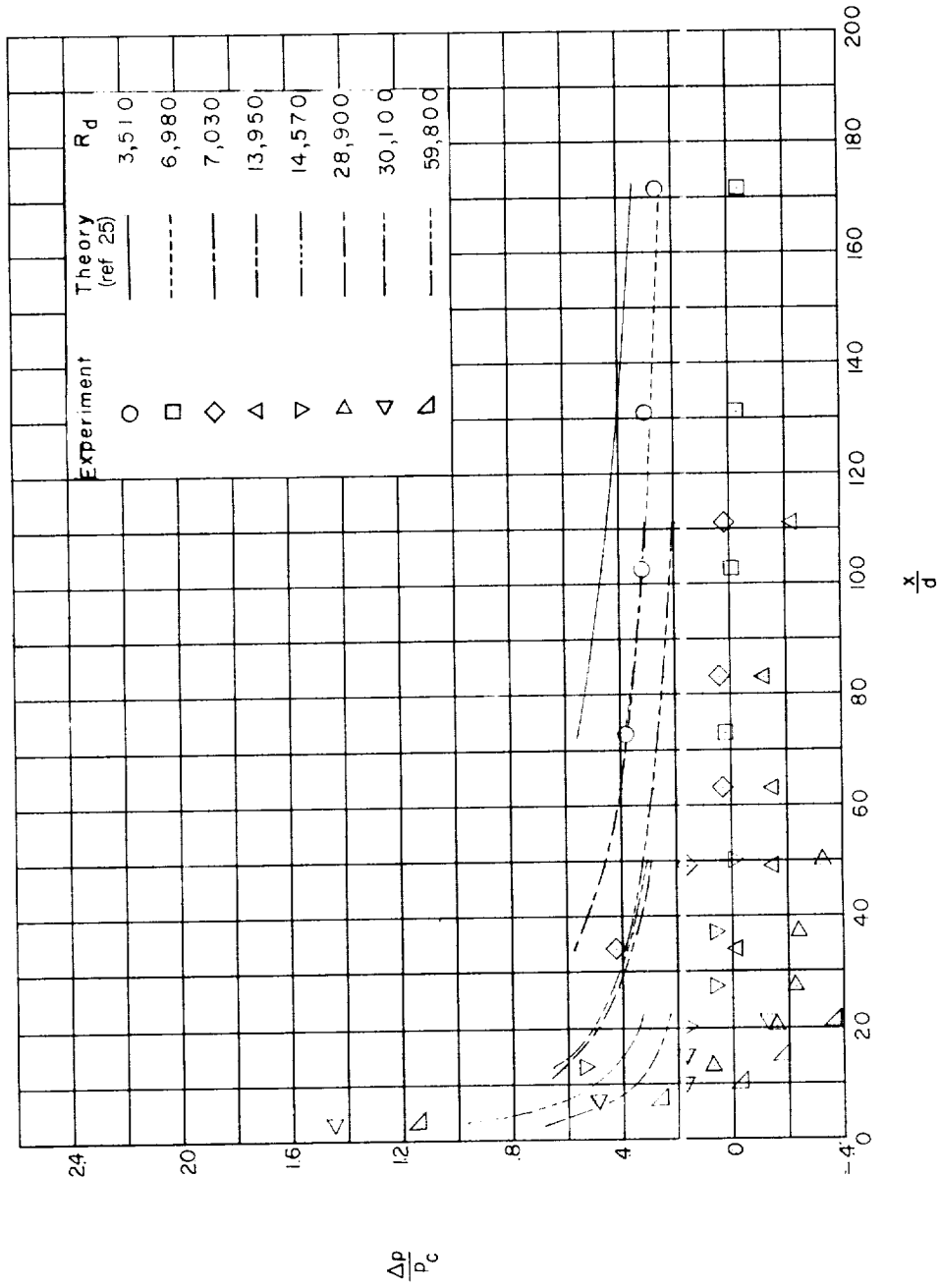
(a) $M_1 = 17$.

Figure 21.- Variation of induced static-pressure ratio with x/d for 5° semiangle cone at various values of R_d.
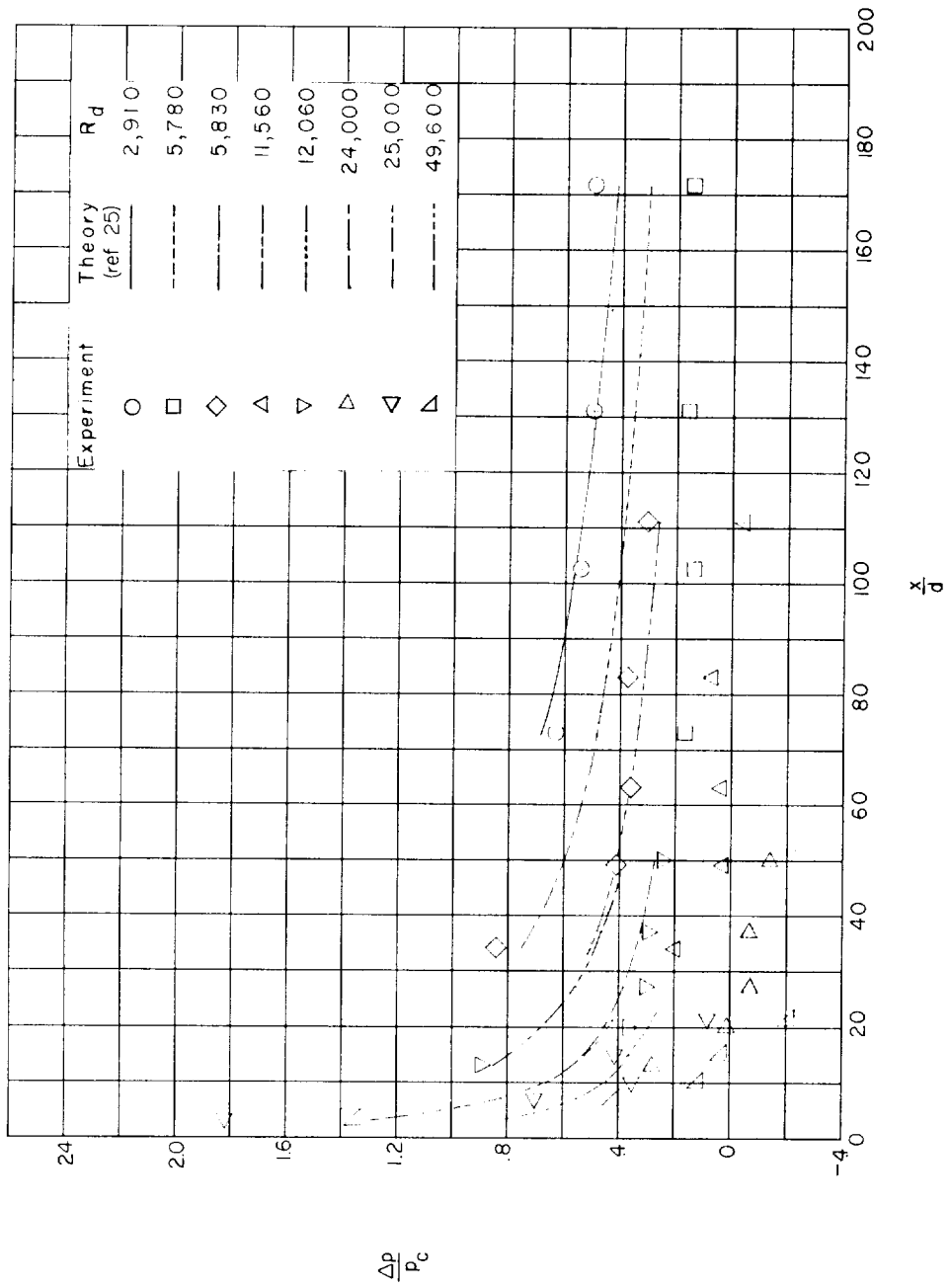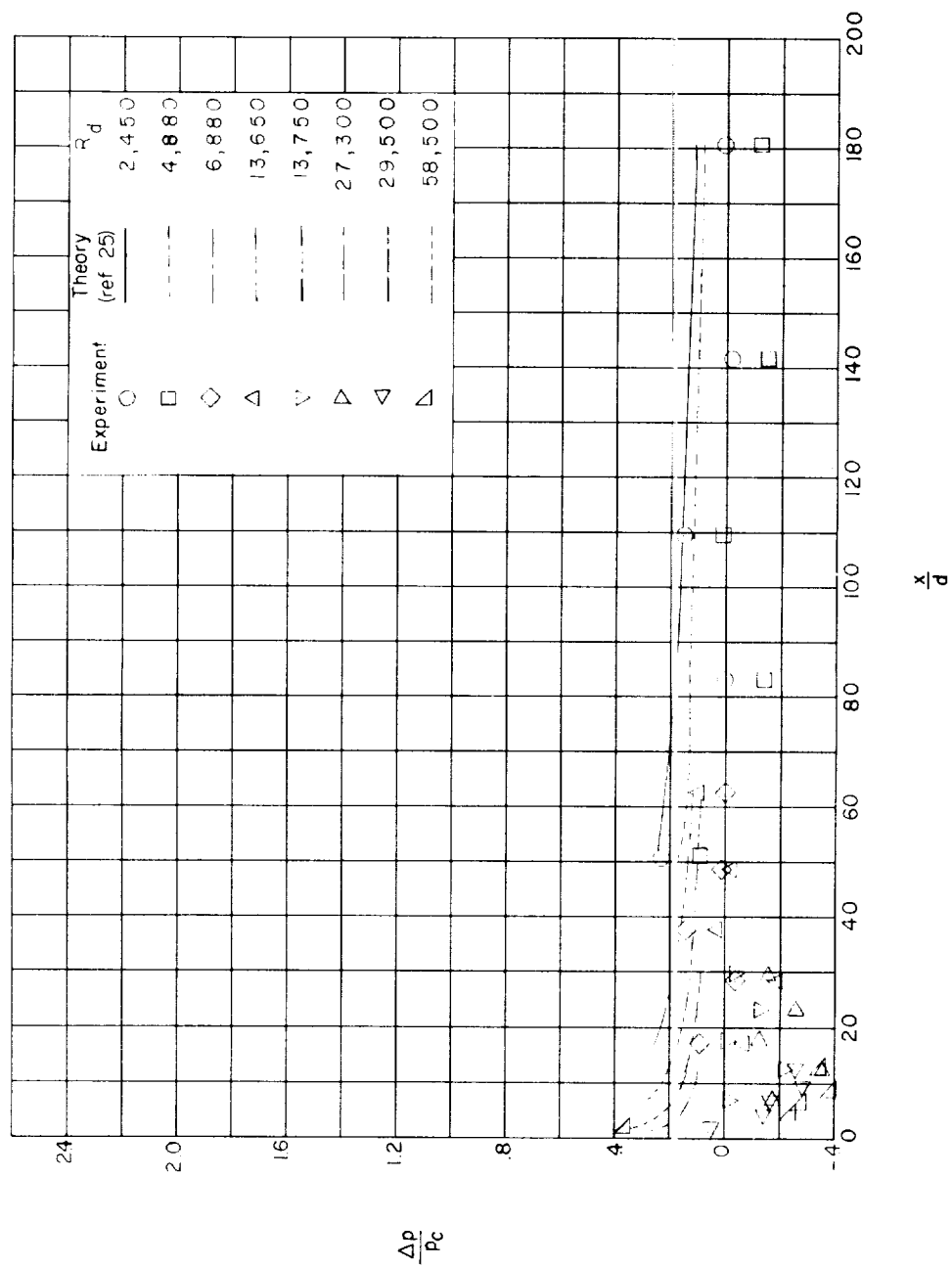
(b) $M_1 = 19$.

Figure 21.- Continued.
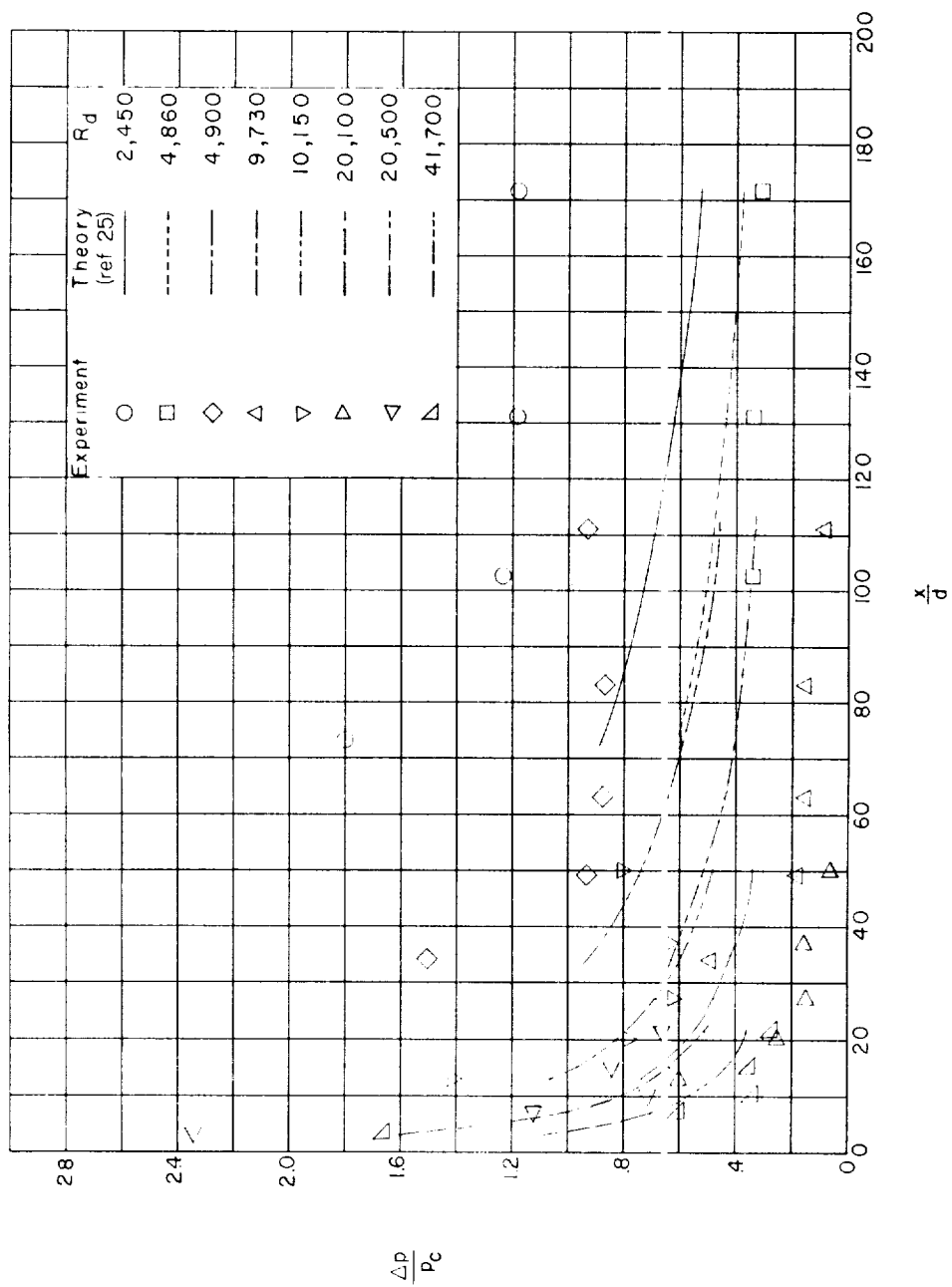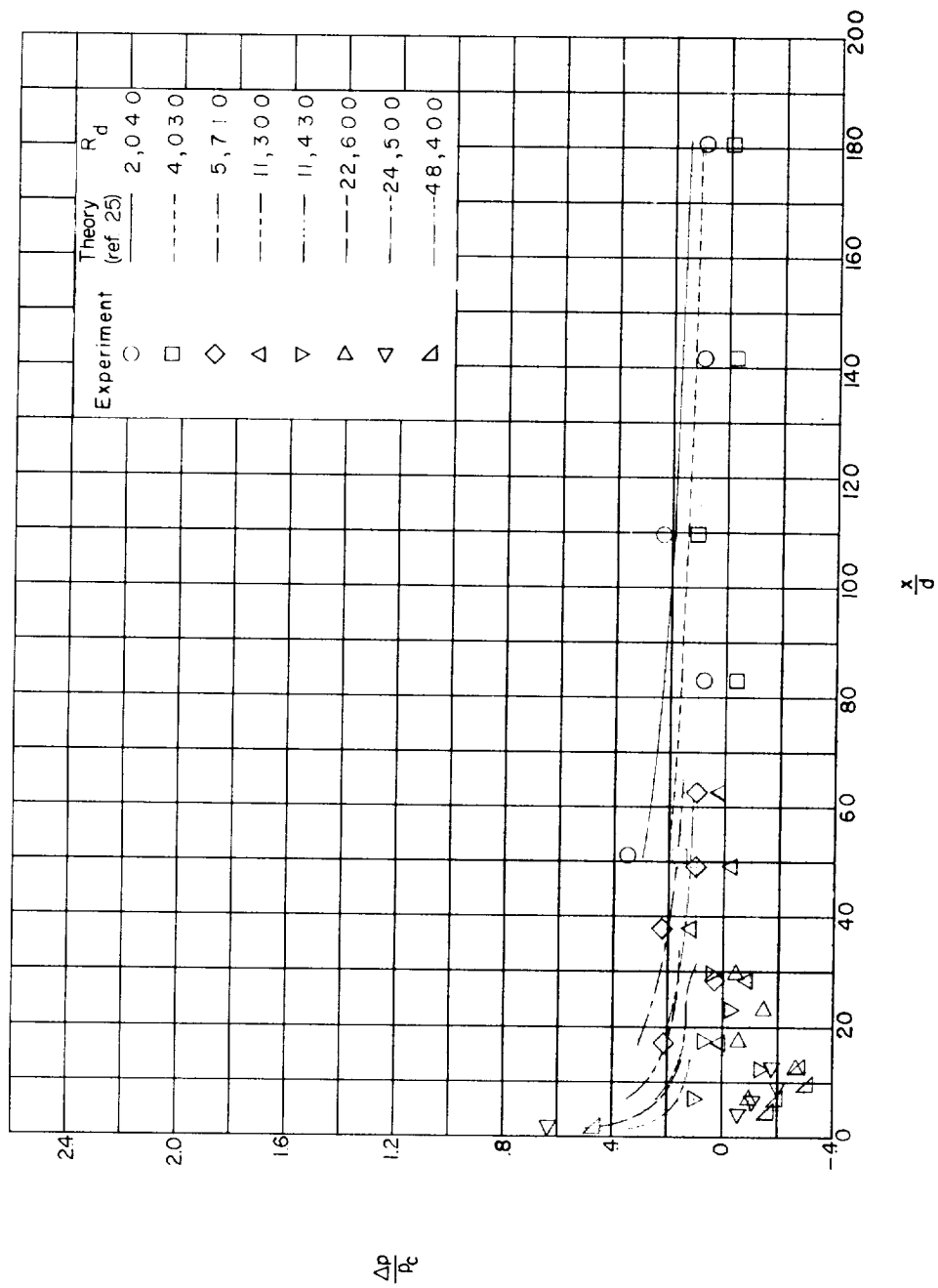
(c) $M_1 = 21$.

Figure 21.- Continued.
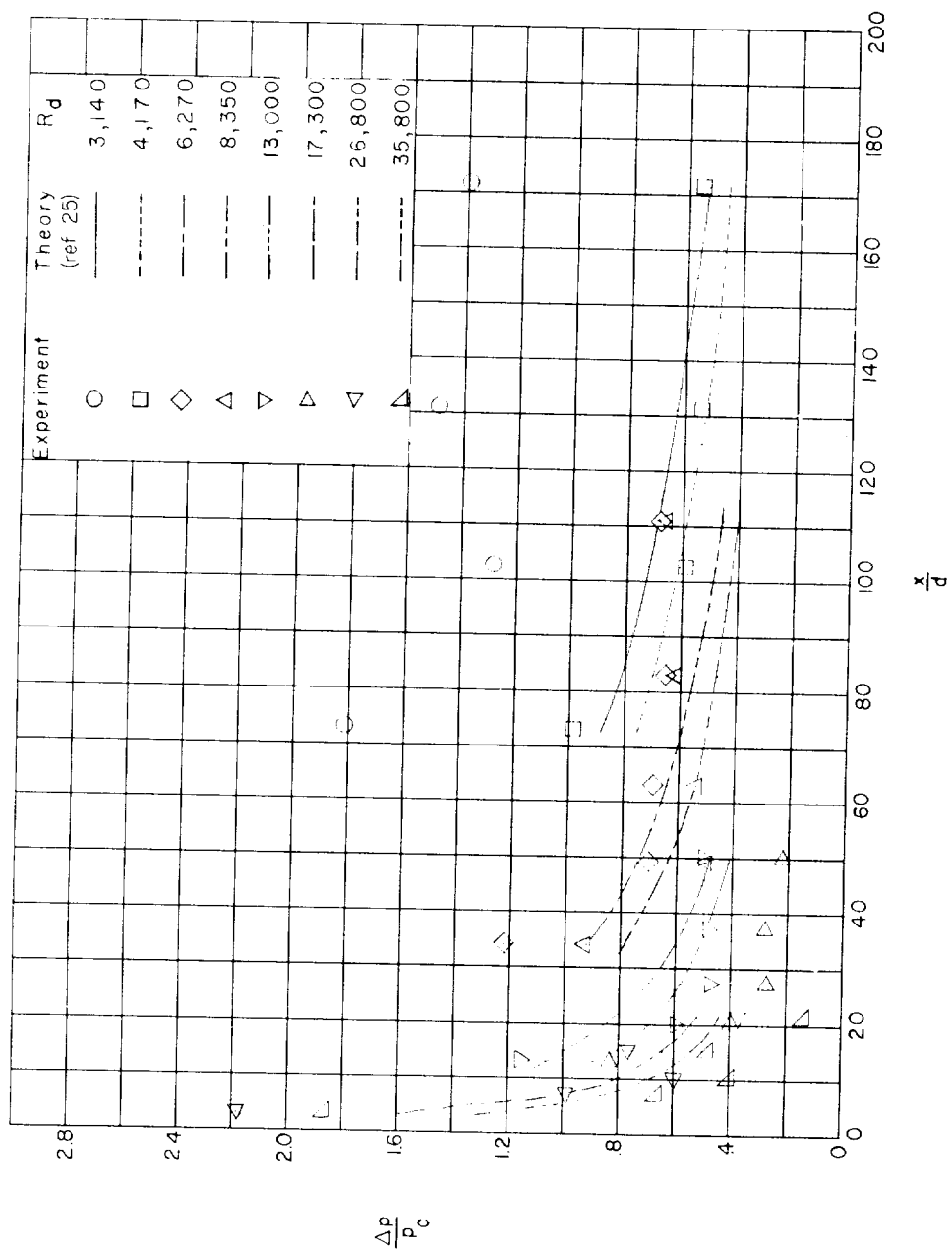
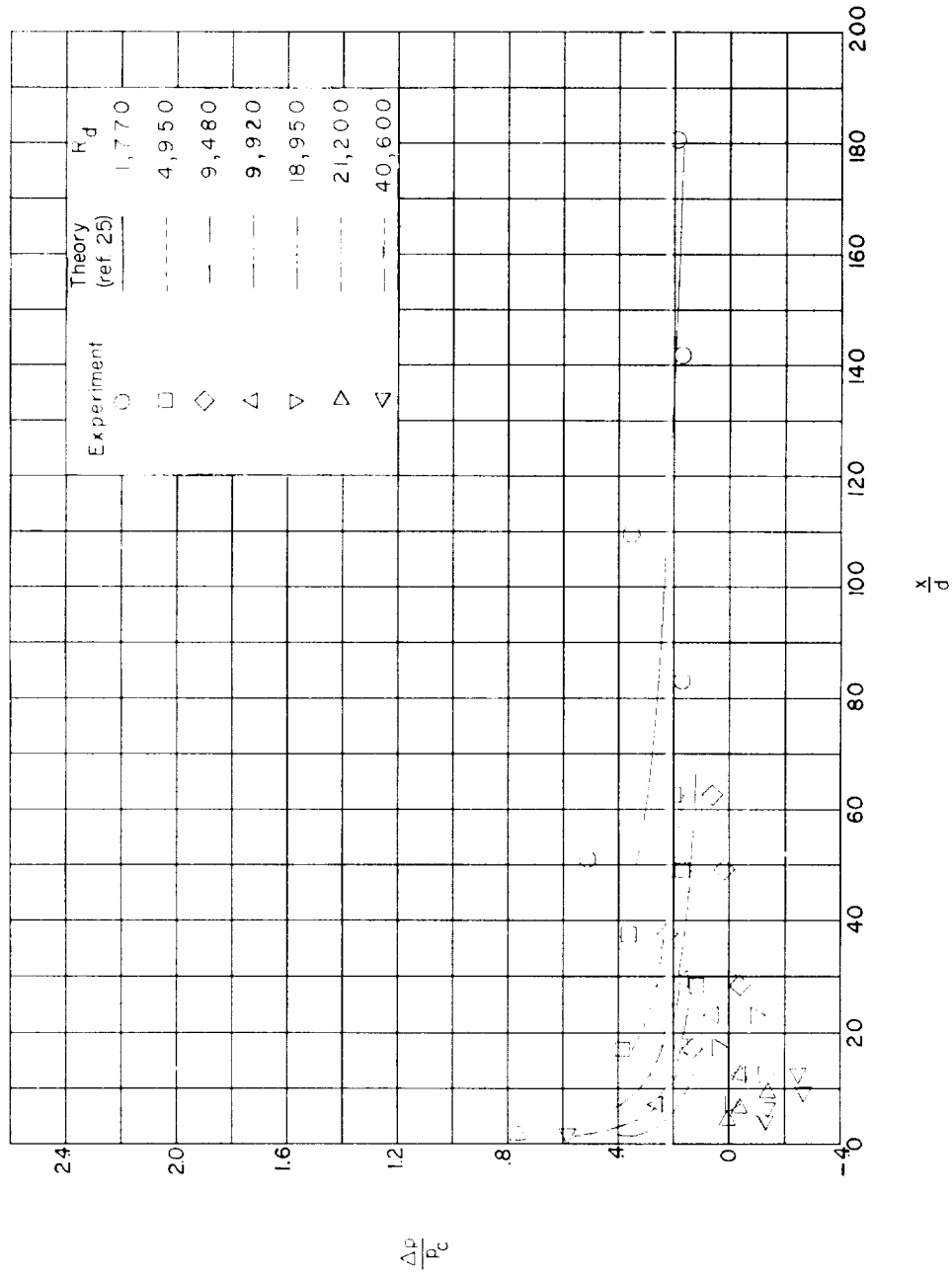(d) $M_1 = 23$.

Figure 21.- Concluded.

(a) $M_1 = 17.$

Figure 22.- Variation of induced static-pressure ratio with x/d for 10^0 semiangle cone at various values of R_d.

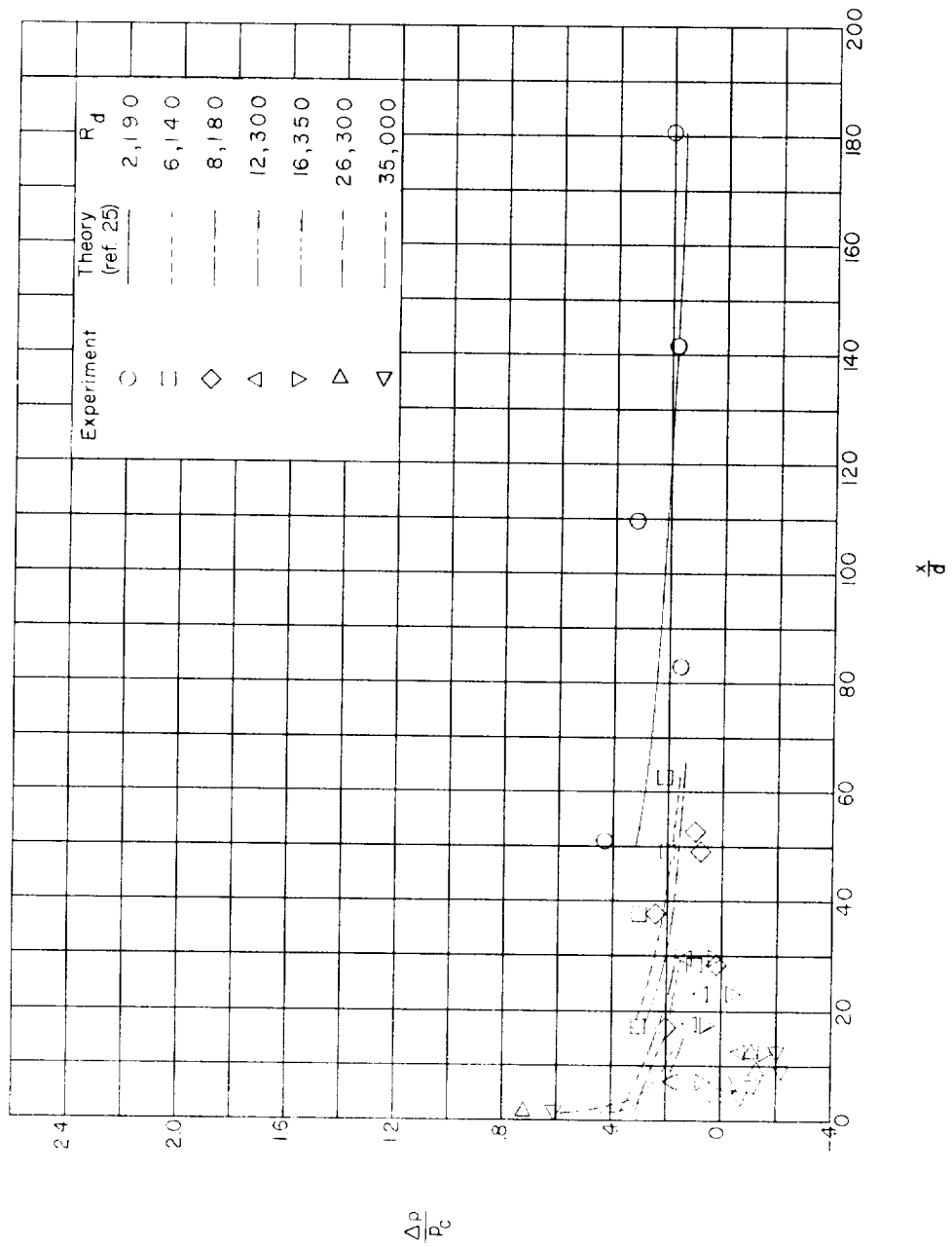(b) $M_1 = 19$.

Figure 22.- Continued.

(c) $M_1 = 21$.

Figure 22. - Continued.

(d) $M_1 = 23$.

Figure 22.- Concluded.